Increased Model Resolution Amplifies Boreal Winter Arctic Precipitation and Atmospheric Circulation Response to Sea Ice Loss

LANTAO SUN,[a] ROBERT C. J. WILLS,[b] CLARA DESER,[c] ADAM HERRINGTON,[c] ISLA R. SIMPSON,[c] AND MELISSA GERVAIS[d]

[a] *Department of Atmospheric Science, Colorado State University, Fort Collins, Colorado*
[b] *Institute for Atmospheric and Climate Science, Department of Environmental Systems Science, ETH Zurich, Zurich, Switzerland*
[c] *Climate and Global Dynamics Laboratory, NSF NCAR, Boulder, Colorado*
[d] *Department of Meteorology and Atmospheric Science, The Pennsylvania State University, University Park, Pennsylvania*

(Manuscript received 8 May 2025, in final form 27 January 2026, accepted 20 February 2026)

ABSTRACT: The impact of future Arctic sea ice loss on local climate and large-scale atmospheric circulation has been extensively studied, including through the Polar Amplification Model Intercomparison Project (PAMIP). However, the influence of horizontal resolution on these responses remains largely unexplored. This study addresses this gap by conducting a set of PAMIP-type experiments in parallel using the Community Earth System Model, version 2.2 (CESM2.2), at global 110-km and Arctic-refined 14-km resolutions, with outputs regridded to a common grid to enable direct comparison. Sea ice loss is identified as the dominant driver of future Arctic precipitation increases in boreal winter. The Arctic-refined model exhibits a larger increase in precipitation over the sea ice loss region compared to the global 110-km model. This amplified response is linked to stronger updrafts and corresponding intensification of upward moisture transport. Additionally, daily precipitation variability increases in response to sea ice loss, with the change in the Arctic-refined model more than twice that in the global 110-km model, primarily connected to enhanced variability in vertical motion. Furthermore, both model resolutions capture Arctic amplification and associated dynamical responses, but the Arctic-refined model shows stronger warming and greater zonal wind deceleration over the polar cap. The thermodynamic budget analysis indicates that transient eddies associated with vertical motion are a major factor in the enhanced warming in the higher-resolution configuration. Collectively, these findings highlight the role of horizontal resolution in shaping Arctic precipitation and atmospheric circulation responses and underscore vertical motion as a key driver of this sensitivity.

SIGNIFICANCE STATEMENT: This modeling study examines how increasing model horizontal resolution influences the atmospheric response to future Arctic sea ice loss. Using the Community Earth System Model, version 2.2 (CESM2.2), we conducted two sea ice loss experiments, one with a typical climate model resolution and one with very high resolution over the Arctic, following an experiment protocol similar to the Polar Amplification Model Intercomparison Project (PAMIP). The results show that higher resolution leads to greater increases in Arctic precipitation and its variability in response to sea ice loss. Additionally, the simulations with high resolution over the Arctic exhibit stronger lower-tropospheric temperature and circulation responses over the polar cap compared to the coarser-resolution simulations. These enhanced responses are likely linked to resolution-dependent differences in vertical motion. Our findings advance the understanding of high-resolution modeling and highlight the critical role of horizontal resolution in accurately simulating climate and climate change in the Arctic.

KEYWORDS: Arctic; Sea ice; Precipitation; Atmospheric circulation; Vertical motion; Climate models

1. Introduction

Arctic sea ice has declined rapidly over the past several decades (Fetterer et al. 2017; Meier and Stroeve 2022). Climate models project a seasonally ice-free Arctic Ocean by the middle of this century under increasing greenhouse gas (GHG) concentrations (Notz and SIMIP Community 2020). Sea ice loss has been identified as the primary driver of Arctic amplification, which is a prominent feature of anthropogenic climate change characterized by the disproportionate surface warming in the Arctic compared to lower latitudes (Serreze et al. 2009; Screen and Simmonds 2010; Rantanen et al. 2022). Numerous studies have highlighted key climate feedbacks driving this amplification (e.g., Pithan and Mauritsen 2014; Stuecker et al. 2018; Feldl and Merlis 2021; Hahn et al. 2021; Previdi et al. 2021; Jenkins and Dai 2021; Taylor et al. 2022; Zhou et al. 2024; Liang et al. 2025) and quantified the contribution of sea ice loss to Arctic warming (Dai et al. 2019; Feldl et al. 2020; Dai and Jenkins 2023; Jenkins et al. 2024). The influence of internal variability on observed and projected polar amplification has also been widely studied (England et al. 2021; Sweeney et al. 2023, 2024; Chen and Dai 2024).

Beyond temperature changes, Arctic precipitation increases at a higher rate (~4.5% per degree of warming) than the

Supplemental information related to this paper is available at the Journals Online website: https://doi.org/10.1175/JCLI-D-25-0260.s1.

Corresponding author: Lantao Sun, lantao.sun@rams.colostate.edu

DOI: 10.1175/JCLI-D-25-0260.1

global-mean precipitation rate (~2%), a phenomenon known as precipitation amplification (Bintanja and Selten 2014; Pithan and Jung 2021). However, the mechanisms and the role of sea ice loss remain uncertain. For example, one proposed mechanism links increased Arctic precipitation to greater evaporation driven by sea ice retreat (Bintanja and Selten 2014). This is consistent with the modeling study by Deser et al. (2010), which found that in response to sea ice loss, the seasonal cycle of Arctic precipitation change closely follows surface energy fluxes. In addition to local evaporation, poleward moisture transport from lower latitudes contributes to the projected increase in Arctic precipitation (Serreze et al. 2024). From an energetic perspective, Anderson et al. (2018) suggested that first-order latent heat release from Arctic precipitation is balanced by the reduced dry static energy convergence. Pithan and Jung (2021) argued that radiative cooling is the primary driver of future Arctic precipitation increases in boreal winter, which can be further linked to Planck and cloud feedbacks (Bonan et al. 2023). In contrast, local evaporation following sea ice retreat was found to play a secondary role in their study. Yukimoto et al. (2024) suggested that increased radiative cooling and reduced dry static energy convergence contributed equally to the recent rise in Arctic precipitation. In addition to changes in mean precipitation, studies have also reported increases in Arctic precipitation variability across different time scales (Pendergrass et al. 2017; Bintanja et al. 2020).

Given the central role of sea ice loss in driving Arctic and broader climate changes, there has been a continued modeling effort to isolate its regional and remote impacts (e.g., Royer et al. 1990; Deser et al. 2010). Arctic sea ice loss can influence Northern Hemisphere (NH) large-scale atmospheric circulation and even global climate through ocean–atmosphere coupling (Barnes and Screen 2015). Modeling studies have also attempted to disentangle the effects of anthropogenic climate change by separating low-latitude warming from polar sea ice loss (McCusker et al. 2017; Hay et al. 2018, 2022), suggesting a tug-of-war between these influences (e.g., Deser et al. 2015). However, the response of midlatitude atmospheric circulation and surface climate to Arctic sea ice loss, particularly over the observational period, remains highly debated (Barnes and Screen 2015; Sun et al. 2016; Blackport and Screen 2019, 2020; Cohen et al. 2020; Dai and Song 2020). Discrepancies among climate models may stem from differences in the magnitude and spatial pattern of sea ice loss (Peings and Magnusdottir 2014; Sun et al. 2015; Koenigk et al. 2016), stratospheric representation (Sun et al. 2015; Zhang et al. 2018), background state (Osborne et al. 2017; Smith et al. 2017), low signal-to-noise ratio (Screen et al. 2014; Mori et al. 2014), and air–sea coupling (Smith et al. 2017; Blackport and Kushner 2018), among other factors (Screen et al. 2018; Smith et al. 2019).

The Polar Amplification Model Intercomparison Project (PAMIP), part of the Coupled Model Intercomparison Project phase 6 (CMIP6), aims to improve scientific understanding of the causes and consequences of polar amplification through a set of coordinated climate model experiments (Smith et al. 2019). These simulations have provided insights into key aspects of the effects of Arctic sea ice loss, including dynamical mechanisms and robustness (Smith et al. 2022), sensitivity to the model's basic state and emergent constraints (Smith et al. 2022; Screen et al. 2022; Simon et al. 2022; Sigmond and Sun 2024), internal variability (Peings et al. 2021; Streffing et al. 2021; Sun et al. 2022), stratospheric pathways (Sun et al. 2022; Liang et al. 2024; Sigmond and Sun 2024), and surface climate responses (Zheng et al. 2023; Ye et al. 2024), as well as the role of ocean–atmosphere coupling (e.g., Kang et al. 2023).

With increasing computational power, recent generations of global climate models have been developed at progressively higher horizontal resolutions (e.g., Caldwell et al. 2019; Chang et al. 2020; Harris et al. 2020), including the creation of kilometer-scale global storm-resolving models (Satoh et al. 2008; Caldwell et al. 2019; Cheng et al. 2022; Hohenegger et al. 2023; Rackow et al. 2025; Segura et al. 2025). A key effort in this advancement is the High-Resolution Model Intercomparison Project (HighResMIP; Haarsma et al. 2016; Roberts et al. 2025), which was established to systematically assess the influence of horizontal resolution on climate simulations using global models at tens-of-kilometer scales. Compared to low-resolution models, high-resolution models can capture fine-scale climate processes more accurately, thereby potentially reducing mean biases (Lu et al. 2015; Moreno-Chamarro et al. 2022; Athanasiadis et al. 2022), improving the representation of climate variability (Smirnov et al. 2015; Larson et al. 2024; Patrizio et al. 2023; Williams et al. 2024; Wills et al. 2024; Sun et al. 2025), and enhancing both decadal climate predictions (Yeager et al. 2023) and long-term projections (Xu et al. 2024). Furthermore, high-resolution models are helping to bridge the long-standing divide between weather and climate research by enabling consistent treatment of mesoscale processes across time scales (Randall and Emanuel 2024).

Global high-resolution models are typically too computationally expensive for long-term climate simulations, particularly for climate processes with inherently low signal-to-noise ratios. In contrast, regional refinement configurations (or global variable-resolution models) provide a more computationally efficient alternative and have been developed for various applications (e.g., Lauritzen et al. 2018; Tang et al. 2023; Lin et al. 2024). These models have been widely used to study extreme convective storms (e.g., derechos; Liu et al. 2023), tropical cyclones (Zarzycki et al. 2014), Greenland's mass balance (Herrington et al. 2022), precipitation and snowpack (Rhoades et al. 2016; Huang et al. 2022), extreme winds (Morris et al. 2024), ocean–atmosphere interactions (Wills et al. 2024), and future Arctic extreme temperature and precipitation changes (Wijngaard et al. 2025). For instance, Herrington et al. (2022) found that the Arctic-refined configuration of the Community Earth System Model, version 2.2 (CESM2.2), produced a more realistic representation of precipitation along the storm track compared to standard low-resolution models. Similarly, Huo et al. (2025) evaluated the Department of Energy's (DOE) Energy Exascale Earth System Model, version 2.1 (E3SMv2.1), with an Arctic regionally refined mesh (25-km atmosphere and land, 10-km ocean–ice) and found reduced biases and improved simulations of Arctic precipitation and

atmospheric circulation. These findings underscore the influence of horizontal resolution on Arctic precipitation and atmospheric circulation.

Modeling studies have consistently demonstrated that precipitation intensity generally increases with horizontal resolution, a relationship often attributed to the sensitivity of vertical motion to grid spacing (Rauscher et al. 2016; Terai et al. 2018; O'Brien et al. 2016; Herrington and Reed 2020; Rasmussen et al. 2023). Using the Boussinesq approximation, Jeevanjee and Romps (2016) provided a theoretical physical basis for this sensitivity, suggesting that resolution-dependent vertical motion arises from scaling arguments for the acceleration of a buoyant air parcel interacting with its environment. Building on this framework, Herrington and Reed (2017, 2018) adopted the Boussinesq approach under the hydrostatic approximation and proposed a power-law scaling of vertical velocity with grid spacing, Δx^n, where $n = -1$. This result contrasts with the earlier scaling analysis by Rauscher et al. (2016), who applied the continuity equation to the spectral properties of horizontal wind and suggested a scaling exponent of $n = -(2/3)$ for horizontal scales of ~100 km or smaller. Herrington and Reed (2020) confirmed the -1 scaling through convergence experiments and further linked the sensitivity of both large-scale and convective precipitation to resolution through the increase in vertical velocity with resolution. However, to our knowledge, few studies have specifically examined how the precipitation response to changes in boundary conditions, such as sea ice loss, varies with horizontal resolution.

The influence of horizontal resolution on the midlatitude response to Arctic sea ice loss has been previously examined by Streffing et al. (2021), who compared three 100-member PAMIP experiments using the Integrated Forecasting System (IFS) at global resolutions of 125, 39, and 16 km, and found no detectable sensitivity. This lack of resolution dependence was attributed to internal atmospheric variability, which can obscure the forced response even in large ensembles (Peings et al. 2021; Sun et al. 2022). However, this single-model result does not rule out resolution-dependent effects, particularly for local responses within the Arctic that may exhibit a higher signal-to-noise ratio (Screen et al. 2013). A more comprehensive assessment remains warranted, with a focus on Arctic precipitation and high-latitude circulation responses, as the former has yet to be explored.

This study investigates the sensitivity of the atmospheric response to future Arctic sea ice loss across different horizontal resolutions and identifies the underlying mechanisms. We use a global atmospheric general circulation model with two different resolutions over the Arctic (110 and 14 km) and conduct a set of parallel PAMIP-type experiments to assess resolution-dependent responses to Arctic sea ice loss, with a focus on Arctic precipitation and high-latitude atmospheric circulation in boreal winter [December–February (DJF)]. The paper is structured as follows: Section 2 details the model experimental design; section 3 presents results on precipitation and atmospheric circulation responses; and section 4 provides a summary and discussion.

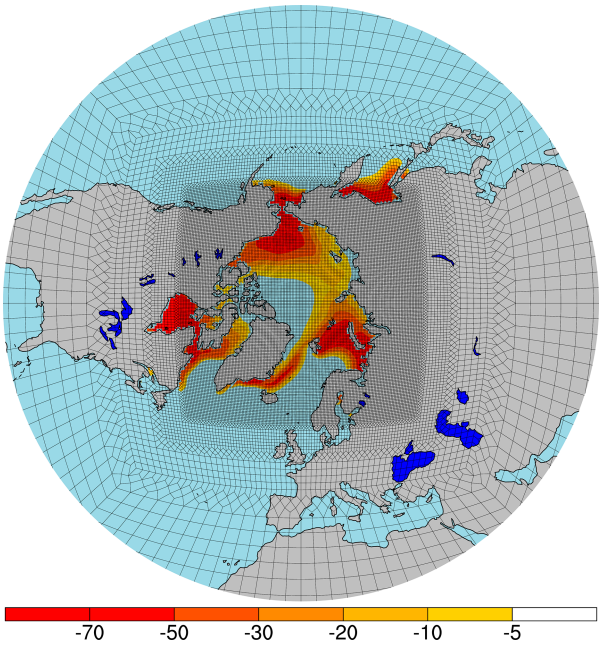

FIG. 1. Arctic-refined CESM grids, with horizontal resolution varying from 14 km in the Arctic (dense hatching) to 110 km in the far field. The shading represents the ensemble-mean change in DJF Arctic sea ice concentration (%) between 1850–69 and 2080–99, based on the ensemble mean of the CESM2-LE dataset.

2. Model experimental design

a. *Model description*

We use the Community Atmosphere Model, version 6.3 (CAM6.3; Craig et al. 2021; Gettelman et al. 2019), which serves as the atmospheric component of the CESM2.2 (Danabasoglu et al. 2020). CESM2 ranks within the top 10% of CMIP-class models in many atmospheric circulation metrics (Simpson et al. 2020). A major update in CAM6's physical parameterizations compared to earlier versions is the cloud layers unified by binormals (CLUBB) scheme (Larson et al. 2002; Bogenschutz et al. 2013), which acts jointly as a planetary boundary layer, shallow convection, and cloud macrophysics scheme. Here, we use CAM6.3 with the spectral-element (SE) dynamical core (Lauritzen et al. 2018), which is capable of regional refinement.

We employ two model resolutions: a standard global uniform-area grid (i.e., ne30pg3_ne30pg3_mg17) with approximately 110-km resolution (global 110-km) and an Arctic-refined grid in which the resolution increases from ~110 to ~14 km over the Arctic (i.e., ne30 × 8_mt12; Arctic 14-km; Fig. 1). Both configurations have the same 32 vertical levels, with a model top at 2.26 hPa (Danabasoglu et al. 2020). The lowest level is located at approximately 60 m above the surface with vertical resolution on the order of ~100 m. Our computational cost analysis on the National Center for Atmospheric Research (NCAR)'s supercomputer Cheyenne shows that the Arctic 14-km model requires approximately 38 times more core hours than the global 110-km model, whereas increasing the global resolution to 14 km results in a much steeper increase—approximately 512 times

more. This underscores that regional refinement is a far more affordable and computationally efficient approach to higher resolution if the resolution over a specific domain is the primary interest.

b. PAMIP-type experimental protocol

We conduct atmosphere-only time-slice experiments similar, but not identical, to the PAMIP protocols (Smith et al. 2019). In all experiments, radiative forcing is fixed at year 2000 levels. Two types of sea ice experiments are conducted: a preindustrial control and a future perturbation, which resemble the PAMIP piSST-piSIC and piSST-futArcSIC experiments, respectively. In the preindustrial control, Arctic sea ice concentration and sea surface temperature (SST) are prescribed from the ensemble mean of 1850–69 averages from the CESM2-Large Ensemble (CESM2-LE; Rodgers et al. 2021). The perturbation experiment follows the same setup but replaces the control Arctic sea ice concentration with its projected 2080–99 average under the shared socioeconomic pathway 3-7.0 (SSP3-7.0) scenario, also from CESM2-LE. In the perturbation experiments, SSTs remain the same as in the control, except in regions where sea ice loss exceeds 10% (~77% of the Arctic Ocean). In these areas, SSTs are set to 2080–99 values to account for both sea ice loss and the associated local SST warming (Smith et al. 2019). Therefore, the surface forcing includes contributions from both reduced ice cover and the accompanying SST increase, rather than sea ice loss alone (Screen et al. 2013).

The projected change in boreal winter (DJF) sea ice concentration from 1850–69 to 2080–99 shows ice loss throughout the Arctic marginal ice zones, with the most pronounced reductions occurring in the Chukchi Sea, Barents–Kara Seas, and Hudson Bay (Fig. 1; color shading). These regions are mostly contained within the 14-km mesh in the high-resolution configuration (Fig. 1; dense hatching). Note that the future Arctic sea ice area loss prescribed in this study is somewhat greater than that used in PAMIP (e.g., 6.5 million km^2 in our simulations compared to 3.5 million km^2 in PAMIP). The choice of a stronger sea ice forcing in this study is intended to maximize the signal, making it easier to detect the sensitivity to resolution.

We first run a 1-yr control simulation and select a mid-September day (18 September) as the initial condition for both the preindustrial control and future sea ice experiments. This timing avoids artificially initializing the stratospheric polar vortex in an anomalously strong or weak state, as the vortex has not yet formed by mid-September (Black et al. 2006). Each experiment runs until the end of February of the following year; outputs from September to November are discarded as spinup. We generate ensembles using the microperturbation method (i.e., "pertlim"), which introduces a small random atmospheric temperature perturbation (on the order of 10^{-14} K) to the initial conditions in each experiment. Due to computational constraints, we run 100 ensemble members for the Arctic 14-km configuration from a single initial condition. For the global 110-km model, we run 600 members in total: 300 members initialized on 18 September of year 1 and an additional 300 members initialized on 18 September of year 2, after extending the control run by one more year. We find modest differences in the stratospheric polar vortex response (~2 m s^{-1} at 10 hPa, 60°N zonal wind) and its downward influence on the troposphere between the two sets of global low-resolution simulations initialized from different years. This resembles the spread seen in Sun et al. (2022), though smaller due to the larger ensemble size used here. These differences likely reflect internal stratospheric variability and its downward coupling (e.g., Streffing et al. 2021; Sigmond and Sun 2024).

c. Model diagnostics and resolution sensitivity assessment

Throughout the paper, comparisons are made between the Arctic 14-km and global 110-km ensembles. In most cases, both model outputs are regridded to a common 0.9° × 1.25° latitude–longitude grid (note that the global 110-km model uses an equal-area grid, not a latitude–longitude grid). For precipitation scaling and decomposition analyses, the native grid is preferred due to its equal-area properties, which simplify area-based calculations. To enable comparison, the Arctic 14-km output is regridded to the native global 110-km grid using the Earth System Modeling Framework (ESMF) first-order conservative remapping algorithm (ESMF Team 2021). Monthly outputs are used in most analyses, except for precipitation scaling and decomposition, which use 6-hourly instantaneous outputs.

The effect of Arctic sea ice loss is isolated by computing the difference between the ensemble means of the future and preindustrial sea ice experiments for each model resolution. A two-sided Student's t test at the 95% confidence level is used to evaluate statistical significance.

3. Results

a. The role of sea ice loss for Arctic precipitation changes

We first examine the role of sea ice loss in future Arctic precipitation changes. Previous work has shown that CAM6, when given prescribed global SST and sea ice anomalies from CESM2-LE, can largely reproduce the late-twenty-first-century Arctic precipitation increase seen in fully coupled simulations (Leister et al. 2025; their Fig. 3). Because we use the same model framework and analyze similar late-century CESM2-LE changes, we can reasonably expect that applying CESM2-LE SST and sea ice anomalies to CAM6 would yield a comparable precipitation response. Comparing our sea ice–only experiments with the CESM2-LE SSP3-7.0 future projection, therefore, provides a useful indication of the importance of sea ice loss in contributing to future Arctic precipitation changes.

The left panel of Fig. 2 shows the boreal winter (DJF) total precipitation change from 1850–60 to 2080–99 under the SSP3-7.0 scenario in CESM2-LE (run at global 1° resolution), alongside the contribution from Arctic sea ice loss, as simulated in the corresponding global 110-km experiment conducted in this work. Over the polar cap (65°–90°N), about 62% of the total precipitation increase in CESM2-LE is attributed to Arctic sea ice loss, rising to 90% poleward of 75°N. When separated by precipitation type, sea ice loss alone

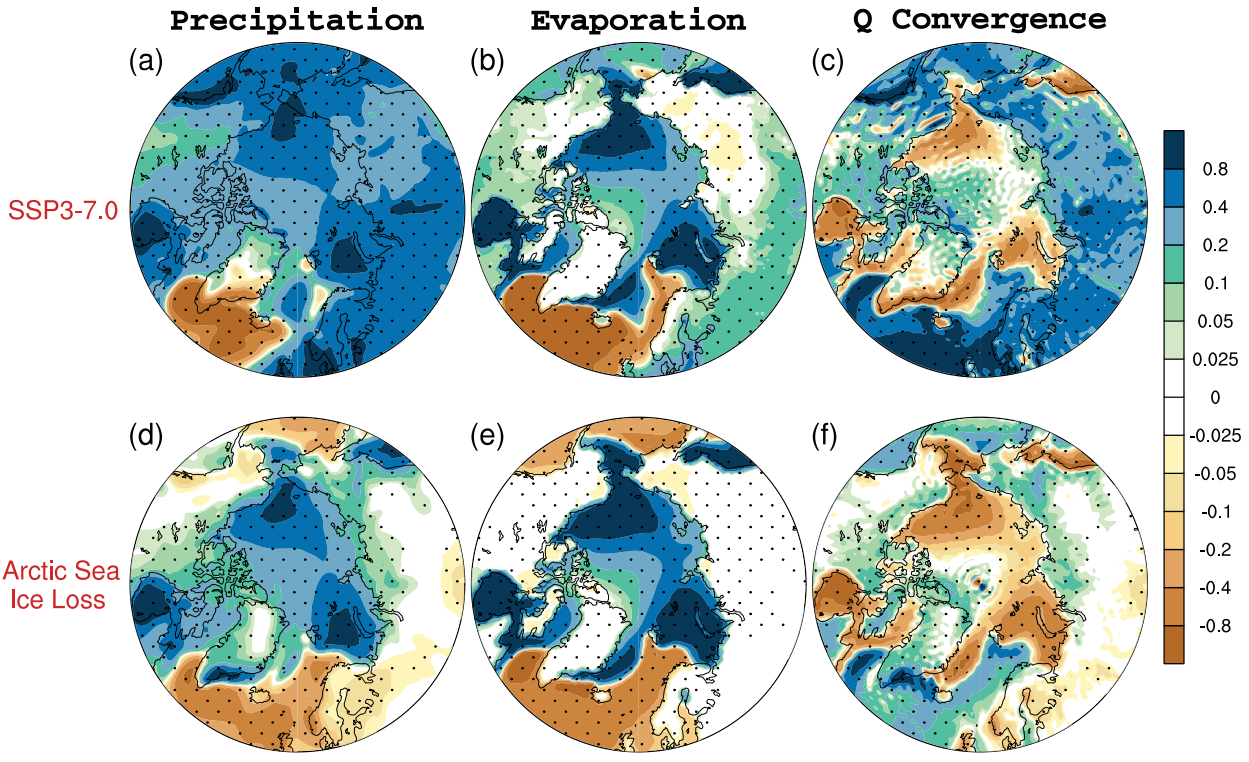

FIG. 2. (left) Precipitation, (middle) evaporation, and (right) moisture convergence difference between 1850 and 1869 and 2080–99 in the CESM2-LE simulations and the response to corresponding Arctic sea ice loss conducted using global 110-km resolution (mm day^{-1}). Stippling indicates regions where the ensemble-mean difference is significantly different from zero at the 95% confidence level based on the two-sided Student's *t* test.

accounts for 57% of the future increase in large-scale stratiform precipitation and the entirety of the increase in parameterized convective precipitation. These results highlight the critical role of sea ice loss in driving future Arctic precipitation increases during boreal winter.

To better understand the mechanism behind the precipitation changes, we analyze the steady-state moisture budget equation:

$$P = E - \nabla \cdot \langle \mathbf{u}q \rangle, \tag{1}$$

where P is the precipitation, E is the evaporation, ∇ is the nabla operator on a sphere, $\mathbf{u}$ is the horizontal wind vector, q is the specific humidity, and $\langle . \rangle$ denotes a density-weighted vertical integral over the atmospheric column. Each term is calculated from monthly output, and the covariance terms (e.g., $\mathbf{uq}$) are available as direct model output, making the residual term negligible (not shown). As shown in the middle and right panels of Fig. 2, the precipitation increase over the sea ice loss region is primarily driven by enhanced evaporation, associated with increased surface latent heat flux. This increase is partially offset by changes in moisture convergence [i.e., the second term on the right-hand side of Eq. (1)]. The consistency in the evaporation and moisture convergence response between future projections using all forcings and sea ice loss experiments implies that this mechanism and the resulting precipitation change can be largely explained by sea ice loss. These findings support the mechanism proposed by Bintanja and Selten (2014), who suggested that future Arctic precipitation increase in boreal winter is mainly due to enhanced local evaporation associated with sea ice retreat, with poleward moisture transport from lower latitudes being less important.

We also examine the energetic constraints on Arctic precipitation changes by analyzing the atmospheric energy budget:

$$L_p = R - \mathrm{DSE}_{\mathrm{adv}} - \mathrm{SH}, \tag{2}$$

where L_p is the latent heat release due to precipitation and R is the radiative cooling of the atmospheric column, defined as the sum of top of the atmosphere (TOA) and surface radiative flux. The $\mathrm{DSE}_{\mathrm{adv}}$ is the dry static energy due to advection, and SH is the surface sensible heat flux. Consistent with previous studies (Pithan and Jung 2021; Bonan et al. 2023), we find that the increase in latent heat release from precipitation in the SSP3-7.0 simulation is primarily balanced by radiative cooling, while changes in surface sensible heat flux and dry static energy largely offset each other. However, our analysis also shows that sea ice loss accounts for the majority of future changes in all three budget terms (Fig. S1 in the online supplemental material), highlighting the central role of sea ice boundary forcing for precipitation changes. This contrasts with Pithan and Jung (2021), who concluded that sea ice retreat and the associated surface flux changes played a secondary role for future Arctic precipitation increases in boreal

TABLE 1. Arctic precipitation climatology and its mean response to sea ice loss during boreal winter (DJF) in global 110-km and Arctic 14-km. The Arctic is defined as 65°–90°N polar cap.

	Mean precipitation climatology (mm day^{-1})			Mean precipitation response (mm day^{-1})		
	Convective	Large scale	Total	Convective	Large scale	Total
(a) Global 110-km	0.030	0.915	0.945	0.042	0.197	0.238
(b) Arctic 14-km	0.013	0.956	0.969	0.012	0.246	0.259
(c) b − a	−0.017	0.041	0.024	−0.030	0.049	0.021

winter. We interpret this apparent discrepancy as evidence that radiative cooling and sea ice retreat are linked processes. Thus, the radiative cooling mechanism does not preclude a key role for sea ice retreat in shaping future Arctic precipitation changes.

b. *Sensitivity of arctic precipitation response at different resolutions*

Next, we examine the sensitivity of Arctic precipitation to horizontal resolution. Table 1 shows the polar cap (65°–90°N) climatological mean precipitation and the mean precipitation response to Arctic sea ice loss in both the global 110-km and Arctic 14-km models. Arctic precipitation is predominantly large scale, accounting for approximately 97% of the climatological total in the global 110-km model and 99% in the Arctic 14-km model. The increase in large-scale precipitation and decrease in convective precipitation at higher resolution align with previous findings (e.g., Terai et al. 2018; Herrington and Reed 2020). Total precipitation in the Arctic 14-km model is only slightly higher (~2.5%) than that in the global 110-km model. In response to Arctic sea ice loss, both large-scale and convective precipitation increase. For both precipitation types, the difference in response between the two models aligns with their climatology, where larger climatological values correspond to larger responses (Table 1 and Figs. 3a–f).

It is worth noting that in the Arctic 14-km model, the "large-scale" precipitation category includes a broader spectrum of resolved motions, capturing smaller-scale features that remain unresolved in the global 110-km model. As a result, a larger proportion of precipitation is classified as large scale in the high-resolution model. This distinction highlights the resolution dependence of process representation: What is treated as parameterized subgrid convection at coarse resolution may become partially resolved at finer resolution. Although 14-km grid spacing is generally considered too coarse to fully resolve deep convection, models at this resolution often begin to exhibit convective behavior without relying entirely on parameterization. These partially resolved convective cores can improve precipitation skill and, in some cases, outperform a purely parameterized convection scheme.

Overall, total precipitation in the Arctic 14-km model increases by about 8.5% more than that in the global 110-km model. The spatial pattern of the mean precipitation response reveals that the largest increases occur over regions of sea ice loss in both models (Figs. 3g–i), consistent with the local increases in evaporation shown previously. The difference between the Arctic 14-km and global 110-km mean precipitation responses is largely uniform across the Arctic.

What leads to the amplified Arctic precipitation response in the Arctic 14-km model compared to the global 110-km model? An analysis of surface energy fluxes shows that their responses are very similar between the two model resolutions (Fig. S2), suggesting that surface forcing does not explain the increased sensitivity. Instead, previous studies have linked daily precipitation to upward moisture flux at the cloud base, following the principle that "what goes up, must come down" (Rauscher et al. 2016). This relationship is described by the approximate scaling equation:

$$P_{\text{tot}} \approx -\frac{1}{g\rho_w}\omega q|_{\text{cb}}, \tag{3}$$

where P_{tot} refers to high-frequency precipitation, $\omega q|_{\text{cb}}$ represents the combined product of ascending motion ω and specific humidity at the cloud base, typically approximated as 850 hPa (e.g., O'Brien et al. 2016), with $g = 9.8$ m s^{-2}, and ρ_w is the density of rainwater (1000 kg m^{-3}). To conduct a similar scaling analysis, we regrid the Arctic 14-km output onto the native global 110-km grid using a conservative remapping method, which allows for direct comparison between the two resolutions.

Figure 4 illustrates the scaling relationship between Arctic precipitation and the corresponding upward moisture flux for both model resolutions using 6-hourly instantaneous data. The scaling relationship remains robust, especially in the global 110-km model. The Arctic 14-km model exhibits a slightly lower slope compared to the global 110-km model but produces higher maximum precipitation, consistent with the notion that increased model resolution generally leads to more intense precipitation. This is primarily due to stronger upward moisture flux associated with enhanced vertical motion, even after regridding to coarse grids. A similar slope behavior was also noted in O'Brien et al. (2016; their Fig. 8), who interpreted slopes less than one as indicative of an effective detrainment flux that removes moisture from cloudy updrafts and reduces precipitation efficiency, though they did not investigate resolution effects. We speculate that a comparable detrainment-related process may contribute to the slope differences across resolutions. Overall, the linear relationship between precipitation and vertical moisture flux at high frequencies raises the question of whether resolution-dependent differences in mean precipitation increases are tied to moisture and/or vertical velocity responses.

Following Herrington and Reed (2020), we decompose spatially averaged precipitation ($\overline{P_s}$) over the polar cap (65°–90°N) as a double sum of the product of the time-mean magnitude

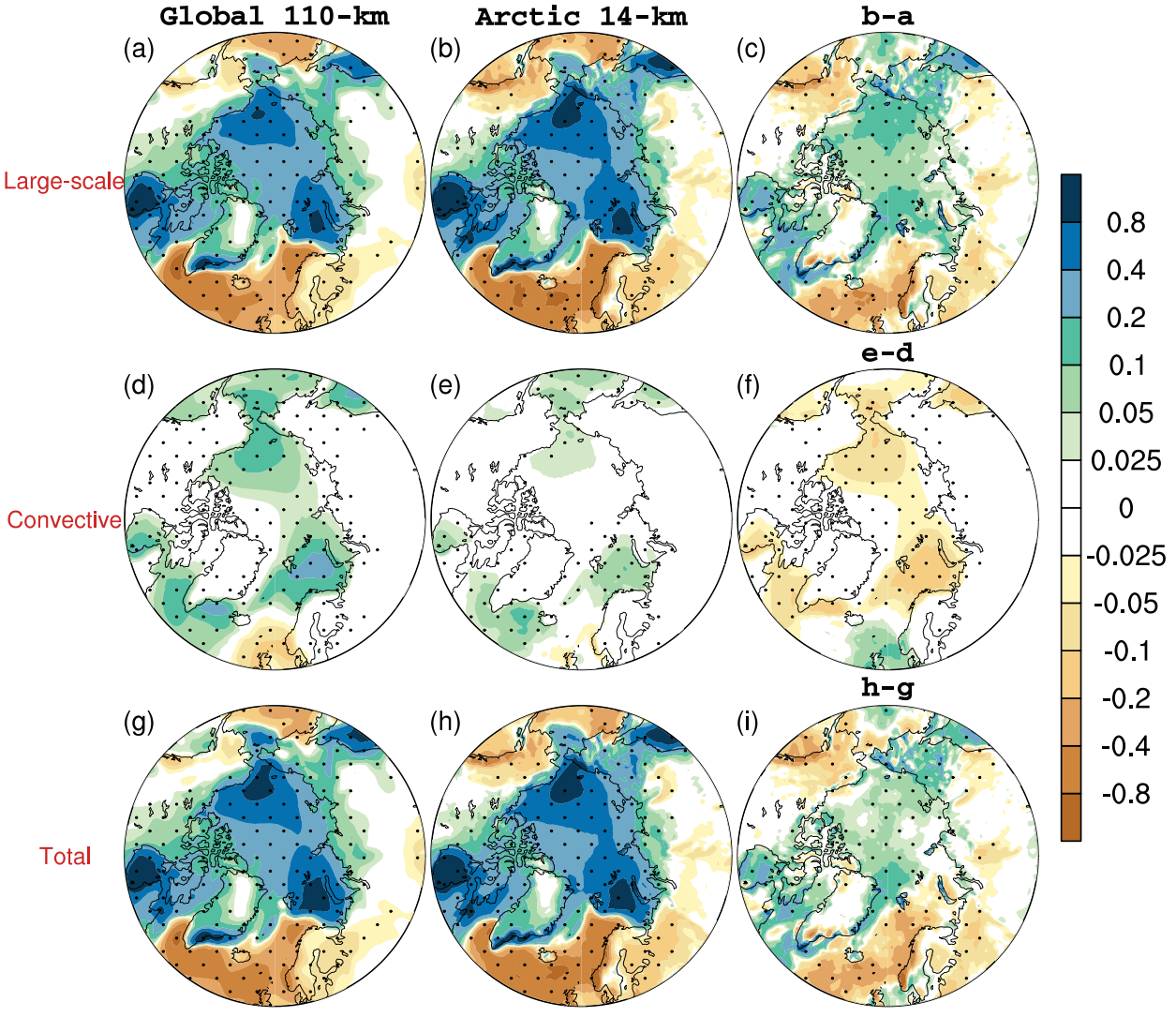

FIG. 3. Mean large-scale, convective, and total precipitation (mm day^{-1}) response to Arctic sea ice loss in (left) global 110-km model, (middle) Arctic 14-km model, and (right) their difference. Stippling indicates regions where the difference between the two ensemble means is statistically significant at the 95% confidence level based on the two-sided Student's t test.

(M_s) and the time-mean spatial frequency (f_s) across ω and moisture space at 850 hPa:

$$\overline{P_s} = \sum_i \sum_j f_s(\omega_i, q_j) M_s(\omega_i, q_j), \tag{4}$$

where ω_i and q_j represent the bins for 850-hPa vertical motion (every 0.1 Pa s^{-1}) and specific humidity (every 0.2 g kg^{-1}), respectively. The f_s measures the occurrence of a particular combination of (ω_i, q_j), while M_s denotes the mean total precipitation associated with that combination of (ω_i, q_j). Thus, the product $f_s M_s$ represents the contribution of each combination (ω_i, q_j) to total precipitation.

Figure 5 shows the magnitude (M_s), frequency (f_s), and their combined product ($f_s M_s$) for Arctic precipitation in both models. In both the Arctic 14-km and global 110-km models, the lowest precipitation magnitude occurs when the vertical motion and specific humidity are near zero. By contrast, heavy precipitation is observed when strong upward motion coincides with high moisture, consistent with the scaling relationship between precipitation and upward moisture flux [Eq. (3) and Fig. 4]. Notably, the distribution in the Arctic 14-km model is broader horizontally than that in the global 110-km model, leading to an increase in heavy precipitation associated with extreme upward moisture flux. This highlights the sensitivity of precipitation to horizontal resolution, particularly in relation to the spectrum of upward motion.

Figure 6 further illustrates this by comparing the probability density functions (PDFs) of Arctic upward motion, moisture, and precipitation at the two resolutions, using 6-hourly instantaneous data. The Arctic 14-km model exhibits stronger upward motion and greater precipitation compared to the global 110-km model. This is consistent with previous findings

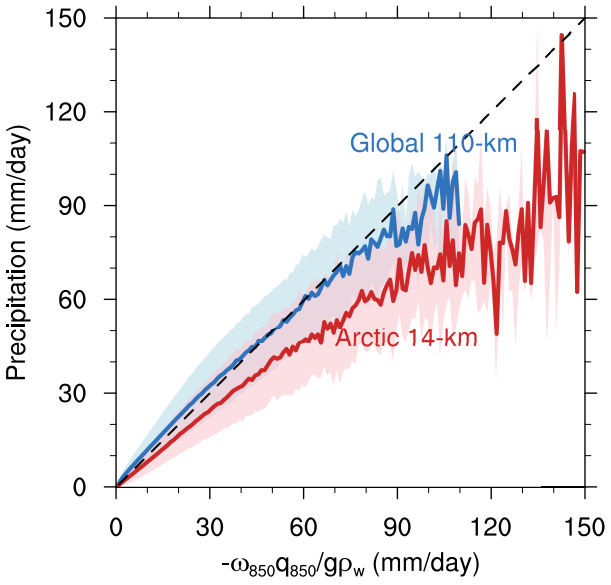

FIG. 4. Arctic precipitation rates vs upward moisture flux at the 850-hPa level during boreal winter (DJF). Solid lines represent the median precipitation rates corresponding to bins of moisture flux, while the shaded areas indicate the interquartile range for each bin. Blue curve indicates the global 110-km model, and red curve indicates the Arctic 14-km output regridded to the global 110-km grid. The dashed line indicates the scaling equation predicted by Rauscher et al. (2016).

that higher-resolution models tend to produce stronger vertical motion and more intense extremes, even after their output is regridded onto a lower-resolution grid (e.g., Herrington and Reed 2020). In contrast, the moisture PDFs are similar between the two resolutions, with the Arctic 14-km model even showing slightly lower moisture values. This suggests that differences in vertical motion, not differences in moisture, explain the sensitivity of precipitation to resolution.

It is also important to note that total precipitation is determined by both the time-mean spatial frequency (f_s) and magnitude (M_s). Extreme precipitation events are rare (see the nonlinear y axis in Fig. 6) and thus contribute minimally to total precipitation. Instead, total precipitation is primarily determined by the frequency distribution, which peaks when vertical motion is near zero, corresponding to low-intensity precipitation events. The Arctic 14-km model exhibits a broader range of vertical motions with a more frequent occurrence of extreme upward motion than the global 110-km model (Figs. 5d–f). As a result, the global 110-km model has a greater contribution from low-intensity precipitation, while the Arctic 14-km model shows a higher contribution from higher-intensity precipitation events (Figs. 5g–i and 6). Therefore, despite similar total precipitation rates, the precipitation distribution differs between the two models, highlighting the sensitivity of precipitation characteristics to horizontal resolution, even after regridding to a common 110-km grid.

Figure 7 shows the combined products (f_sM_s) of total precipitation response to Arctic sea ice loss, along with its individual contributions from changes in frequency, magnitude, and their covariance, as described by the following equation:

$$\Delta\overline{P_s} = \sum_i\sum_j \Delta(f_sM_s) = \sum_i\sum_j \Delta f_sM_s + \sum_i\sum_j f_s\Delta M_s + \sum_i\sum_j \Delta f_s\Delta M_s\,. \quad (5)$$

In response to Arctic sea ice loss, the contribution to total precipitation from conditions when moisture exceeds 0.5 g kg^{-1} increases and the contribution from conditions when it falls below this threshold decreases, which is consistent with a moisture-availability increase associated with newly ice-free ocean, even though it does not reveal the accurate dynamics of the precipitation (e.g., vertical motion during cold-air outbreaks). The change in the precipitation frequency–magnitude distribution is primarily explained by changes in frequency, with the increase partly offset by a decrease in magnitude and, to a lesser extent, by changes in the covariance between frequency and magnitude. Additionally, the stronger vertical motion in the Arctic 14-km model leads to increases in frequency across a broader range of vertical motions, explaining the overall larger precipitation increase in the Arctic 14-km model (Figs. 7c,f).

Arctic sea ice loss not only increases mean precipitation but also alters daily precipitation variability. Table 2 presents the climatological daily precipitation standard deviation, computed at each location and then averaged over the polar cap, along with its response to Arctic sea ice loss in both resolutions. The Arctic 14-km model exhibits only a slightly higher daily precipitation variability (~6%) compared to the global 110-km model. However, in response to sea ice loss, the increase in daily variability in the Arctic 14-km model is more than twice that of the global 110-km model, highlighting a strong sensitivity to model resolution.

The top row of Fig. 8 shows the spatial distribution of the response in daily precipitation standard deviation for both models and their differences, indicating that regions with substantial sea ice loss experience the largest increases in variability. Both models exhibit similar spatial patterns, with the Arctic 14-km model showing a greater magnitude of increase; the difference between the models is nearly uniform across the Arctic. In contrast, near-surface temperature variability shows no clear sensitivity to resolution, with both models exhibiting similar decreased daily temperature variability (not shown).

What causes daily precipitation variability to respond more strongly to Arctic sea ice loss in the high-resolution model compared to the low-resolution model? Recall that Arctic precipitation can be approximated by upward moisture flux [Eq. (3) and Fig. 4]. Indeed, the sensitivity of daily precipitation variability can also be attributed to vertical moisture flux variability (Figs. 8d–f). Notably, the response magnitude of vertical moisture flux variability in the Arctic 14-km model exceeds that of precipitation variability response, resulting in a larger difference between the models (cf. Figs. 8a–f). This happens because the slope of the precipitation-to-upward moisture flux relationship is less than one in the Arctic 14-km model (Fig. 4), necessitating a larger increase in vertical moisture

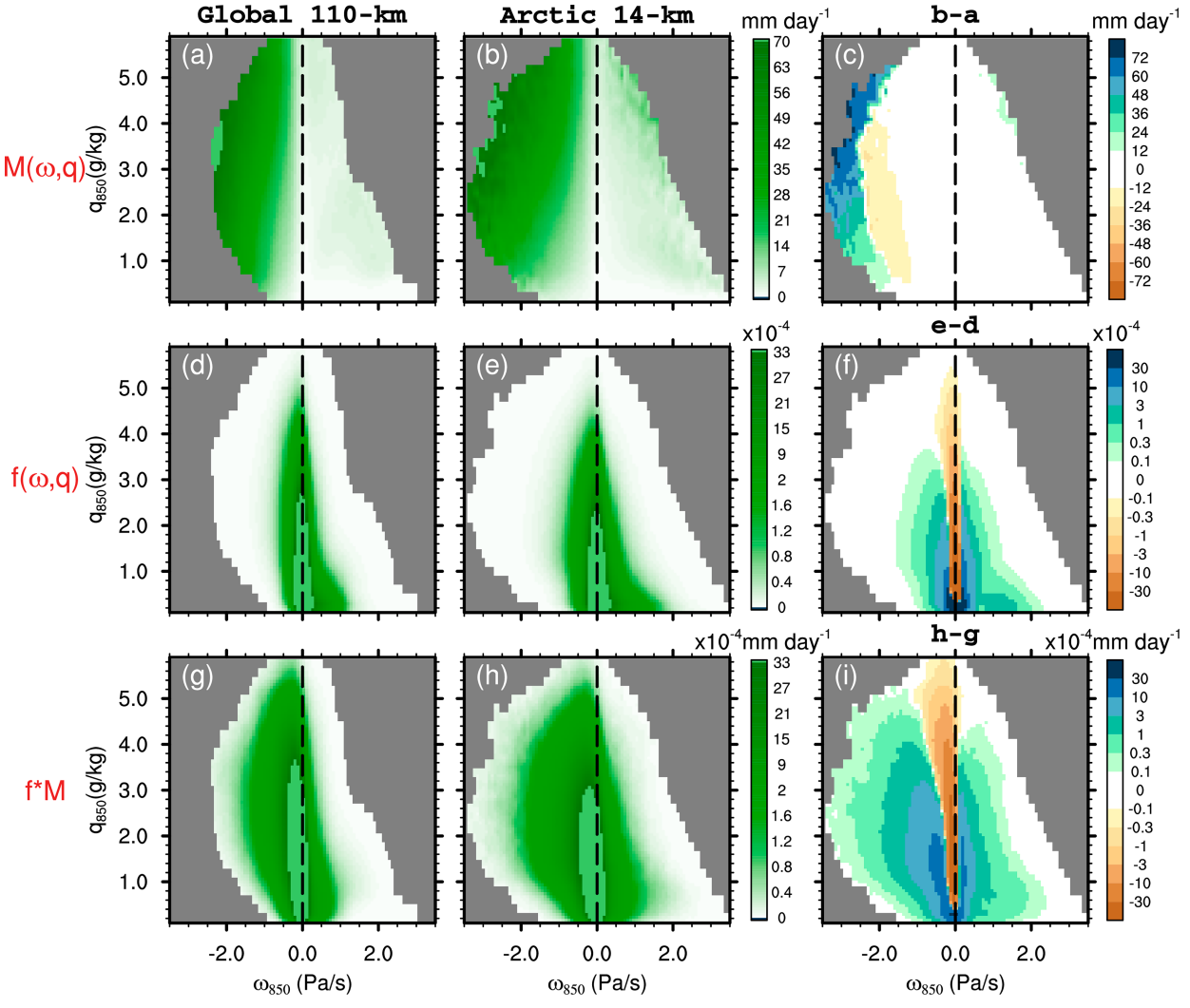

FIG. 5. Decomposition of the Arctic climatological total precipitation rates into contributions from ω_{850} and q_{850} environmental conditions shown for (left) global 110-km control, (middle) Arctic 14-km control, and (right) their difference. The Arctic 14-km output has been regridded to the native global 110-km grid. (top) The time-mean magnitude term $M(\omega_i, q_j)$ and (center) the space–time frequency term $f(\omega_i, q_j)$. (bottom) The magnitude term multiplied by the space–time frequency term. Integrals over $f(\omega_i, q_j)M(\omega_i, q_j)$ give the climatological, area-averaged total precipitation rate. Gray shading indicates areas with no bins in the combined ω_{850}–q_{850} space. Note that the color scales for the middle and bottom rows are nonlinear.

flux variability to produce the observed precipitation response. Nevertheless, the relationship between precipitation and vertical moisture flux holds for daily variability.

To further investigate the sensitivity of daily precipitation variability to model resolution, we show vertical motion and moisture variability in the bottom two rows of Fig. 8. Vertical motion exhibits a similar sensitivity as vertical moisture flux, with a larger increase in variability in the high-resolution model compared to the low-resolution model. This contributes to the greater increase in precipitation variability in the Arctic 14-km model relative to the global 110-km model. In contrast, moisture variability shows little signal over the Arctic. However, sea ice loss enhances mean moisture over the Arctic (Fig. 7), with a slightly larger magnitude in the high-resolution model. As a result, an equivalent change in vertical motion variability leads to a larger increase in vertical moisture flux variability, helping to explain part of the resolution-dependent difference in precipitation variability.

c. *Sensitivity of atmospheric circulation response at different resolutions*

We now turn to the atmospheric circulation response to Arctic sea ice loss. Figure 9 shows the boreal winter zonal-mean temperature and zonal wind responses (shading) in the Arctic 14-km and global 110-km configurations, along with their differences, overlaid with their climatology (contours). Both models exhibit strong surface-intensified Arctic amplification in the lower troposphere in response to sea ice loss,

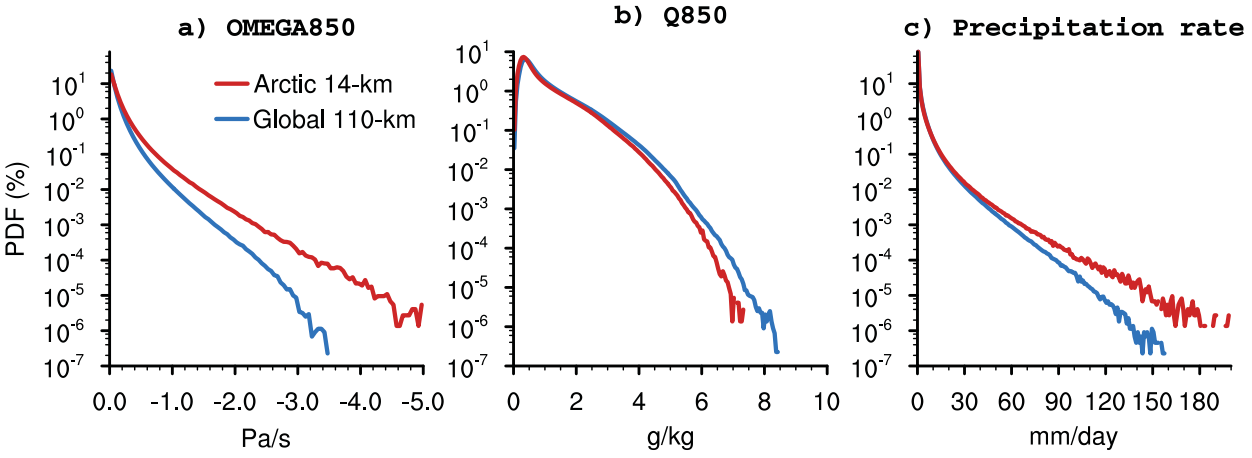

FIG. 6. PDFs of the Arctic upward ω_{850}, q_{850}, and total precipitation rate for the control simulations in the global 110-km and Arctic 14-km models. The Arctic 14-km output has been regridded to the native global 110-km grid.

accompanied by modest warming in the polar stratosphere. Warming in the Arctic 14-km model is slightly stronger than in the global 110-km model throughout the troposphere, with a maximum difference of about 1 K around 800 hPa. Consistent with thermal wind balance, zonal-mean zonal winds show a strong deceleration centered around 60°N throughout the free troposphere and lower stratosphere in response to Arctic sea ice loss, with a weak but statistically significant strengthening around 35°N, in both models. The magnitude of the deceleration is approximately 50% larger in the Arctic 14-km model compared to the global 110-km model (peak values of 1.90 m s^{-1} compared to 1.25 m s^{-1} at upper levels), consistent with the greater tropospheric warming response.

The spatial distributions of the temperature response at 800 hPa and the zonal wind response at 500 hPa in the two models are compared in Fig. 10. In response to sea ice loss, both models show a significant temperature increase throughout the Arctic, with the largest warming centered over major ice loss regions such as Hudson Bay and the Barents–Kara Seas and a significant zonal wind decrease between 65° and 80°N and increase at lower latitudes, indicative of a southward shift of the Atlantic jet and a strengthening of the Pacific jet. These results are largely consistent with previous modeling studies (Ronalds et al. 2020; Peings et al. 2021; Yu et al. 2024). Compared to the global 110-km model, the Arctic 14-km model shows enhanced warming over the central Arctic and slight cooling over the high-latitude continents (particularly central–eastern Canada, central Europe, and eastern Russia), accompanied by a more pronounced zonal wind deceleration along the Arctic coastline, particularly in the Eurasian sector, and a small increase over eastern Canada and the Mediterranean Sea (Figs. 10c,f).

Figure 11 shows the geopotential height response at 500 and 1000 hPa, along with the differences between the two models. In response to sea ice loss, upper-level geopotential height increases over the Arctic and decreases over the Pacific and Atlantic–Europe sectors. In contrast, near-surface geopotential height exhibits a zonal-wave-1 pattern at high latitudes, with positive anomalies over the Eurasian continent and Greenland and negative anomalies over North America and the Pacific Ocean. These features are consistent with previous modeling results (e.g., Deser et al. 2016; Smith et al. 2022). Consistent with the stronger Arctic warming in the Arctic 14-km model, its 500-hPa geopotential height response is also more pronounced over the central Arctic, with weak negative anomalies over eastern Canada and Europe. Collectively, while these statistically significant response differences may project onto the negative phase of the North Atlantic Oscillation (NAO; Hurrell 1995) or the Northern Annular Mode (NAM; Thompson and Wallace 2000), they do not fully resemble the canonical NAO/NAM patterns, as the signals are primarily confined to the polar regions.

Previous studies have identified substantial internal variability in the effects of Arctic sea ice loss and suggested that at least 200 ensemble members are needed to robustly isolate the forced response (Labe 2020; Peings et al. 2021; Sun et al. 2022). Given that our Arctic 14-km ensemble is limited to 100 members, we further examine the response uncertainty through random sampling techniques. To do this, we follow Deser et al. (2017) and apply a bootstrapping method (Mudelsee 2010) to the polar-cap (65°–90°N) temperature at 800 hPa. We randomly sample 100 members from both the control and the future sea ice experiments for both resolutions with replacement and repeat this process 1000 times. Figure 12 shows the distribution of the differences in polar temperature responses in the two models based on randomly sampled 100-member averages. Depending on the members sampled, the magnitude of the response difference varies between 0.2 and 0.8 K (Fig. 12a). However, the response difference consistently shows relative warming in the Arctic 14-km model across all 1000 iterations, indicating that the enhanced warming in the high-resolution model compared to the low-resolution model is a robust feature. We suspect that this might be related to the fact that local response within the Arctic tends to have a larger signal-to-noise ratio than the remote ones (e.g., midlatitude response discussed in Streffing et al. 2021).

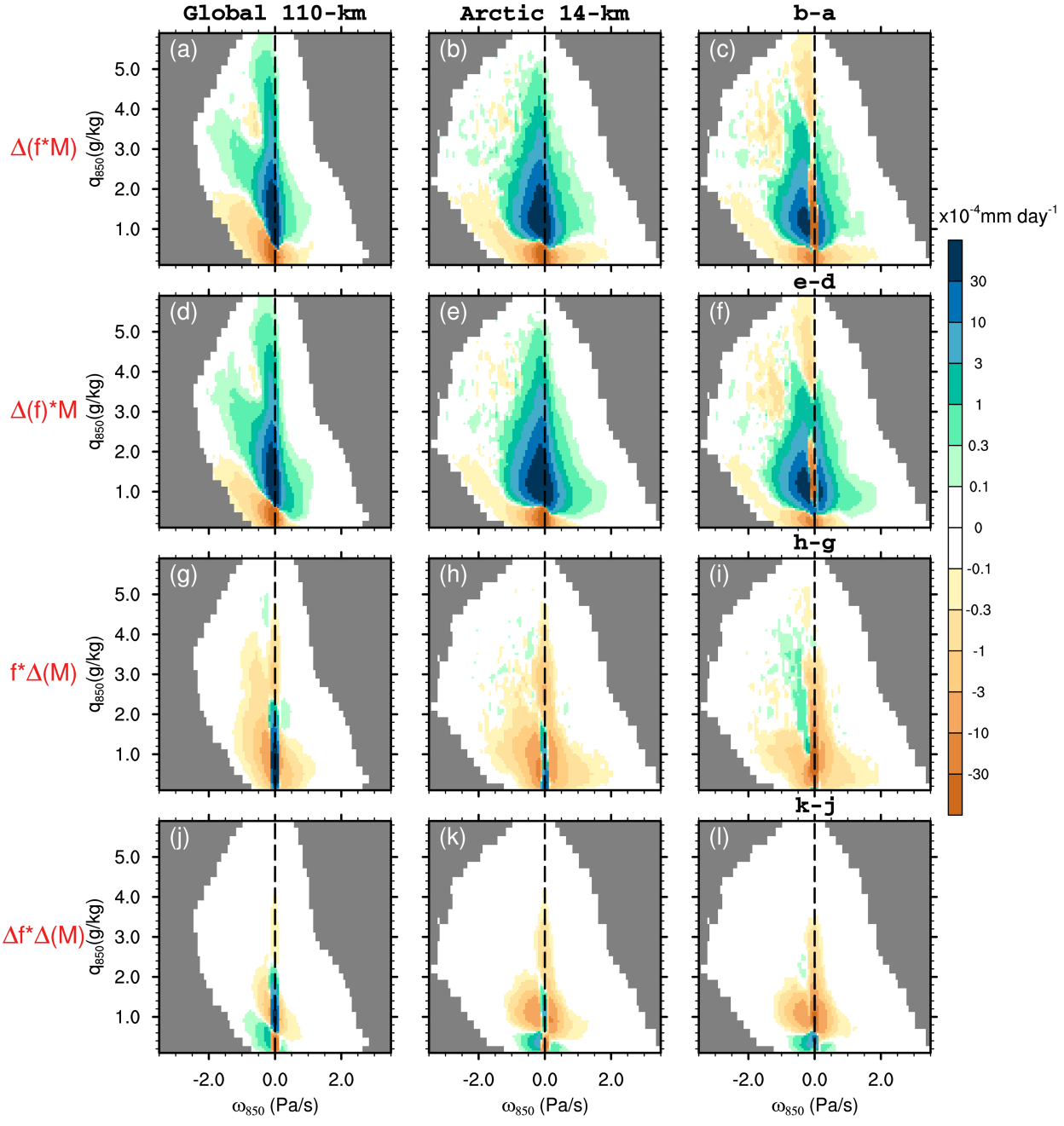

FIG. 7. As in Figs. 5g, 5h, and 5i, but showing the response to Arctic sea ice loss for the (a)–(c) magnitude multiplied by space–time frequency term [i.e., $f(\omega_i, q_j)M(\omega_i, q_j)$], (d)–(f) magnitude multiplied by change in frequency, (g)–(i) change in magnitude multiplied by frequency, and (j)–(l) change in magnitude multiplied by change in frequency. Panels (c), (f), (i), and (l) show the difference between the global 110-km and Arctic 14-km models. The Arctic 14-km output has been regridded to the native global 110-km grid. Gray shading indicates areas with no bins in the combined ω_{850}–q_{850} space. Note that the color scales are nonlinear.

Another key question is whether the distributions of the temperature and circulation responses are connected. To investigate this, we applied the same selection procedure to the 500-hPa geopotential height and zonal wind responses and generated scatterplots of the 100-member ensemble-mean response differences of these variables (Figs. 12b,c). As expected, the polar-cap-averaged geopotential height and the 65°–80°N zonal wind response differences are correlated with the temperature response, with correlation coefficients of 0.65 and 0.44, respectively. This indicates that variations in geopotential height and zonal wind response differences are closely linked to the magnitude of tropospheric warming. Additionally, we

TABLE 2. As in Table 1, but for the Arctic daily precipitation standard deviation and its response to Arctic sea ice loss.

	Daily precipitation variability climatology (mm day^{-1})	Daily precipitation variability response (mm day^{-1})
(a) Global 110-km	1.34	0.08
(b) Arctic 14-km	1.42	0.19
(c) b − a	0.08	0.11

constructed composite response differences between the Arctic 14-km and global 110-km models for the 5th–10th and 90th–95th percentiles of the 800-hPa temperature, 500-hPa geopotential height, and 500-hPa zonal wind. The results reveal similar spatial patterns, though the magnitudes of the dynamical responses vary (Figs. S3).

To further investigate the mechanism behind the temperature response differences between the Arctic 14-km and global 110-km models, we perform a thermodynamic budget analysis for the polar-cap temperature tendency at 850–300 hPa using the model's 0.9° × 1.25° hybrid-coordinate output, following the method of Wills et al. (2024). The time-mean thermodynamic equation is given by

$$\underbrace{\overline{Q_{\text{latent}}}}_{Q_L} + \underbrace{\overline{Q_{\text{rad}} + Q_{\text{turb}}}}_{Q_R} - \underbrace{\nabla_y \cdot \overline{v'T'}}_{\text{TE}_y} - \underbrace{\left[\partial_p \overline{(\omega' T')} - \kappa \frac{\overline{(\omega' T')}}{p}\right]}_{\text{TE}_p} - \underbrace{\overline{u} \nabla_x \overline{T}}_{A_x} - \underbrace{\overline{v} \nabla_y \overline{T}}_{A_y} - \underbrace{\left(\overline{\omega} \partial_p \overline{T} - \kappa \frac{\overline{\omega}\,\overline{T}}{p}\right)}_{A_p} = 0, \quad (6)$$

where Q_L represents the latent heating term and Q_R denotes the sum of radiative heating and heating by the turbulence parameterization. The TE_y and TE_p correspond to transient eddy meridional wind and vertical motion terms, respectively, due to all resolved departures from the coarse-grained time mean. The A_x, A_y, and A_p represent the zonal, meridional, and vertical dynamical contributions, with A_p including both vertical advection and adiabatic heating. Assuming equilibrium, the sum of these terms is zero. The residual, due to interpolation, is smaller than any of the other terms and is not shown.

Figure 13 shows the climatology and response to Arctic sea ice loss for each term in Eq. (6) averaged over the polar cap in the free troposphere (300–850 hPa). The climatology in both the Arctic 14-km and global 110-km models is governed by a balance between radiation cooling (Q_R) and heating from condensation (Q_L), mean advection (A_x, A_y, and A_p), and transient-eddy heat fluxes (TE_y and TE_p) (Fig. 13a). The response to Arctic sea ice loss in both models is primarily driven by latent heat release from increased precipitation (Q_L), with smaller contributions from enhanced subsidence heating (A_p) and transient-eddy vertical heat flux (TE_p), and balanced by increased radiative cooling (Q_R) and reduced transient-eddy meridional heat flux (TE_y), all of which are consistent with a warming-driven adjustment (Fig. 13b). Although the precipitation increases more in the Arctic 14-km model (Fig. 3), the increase in latent heating above 850 hPa does not exceed that in the global 110-km model, likely because condensation occurs primarily near the surface. In comparison, the largest positive warming tendency difference between the Arctic 14-km and global 110-km responses is found in the transient-eddy vertical heat flux term (TE_p), suggesting that enhanced transient-eddy vertical heat transport may play a causal role in the larger warming response observed in the Arctic 14-km model.

We also repeat the budget analysis for the whole atmospheric column and find similar results, although the contribution of TE_p becomes secondary to that of A_p in explaining the warming tendency difference between the two models (not shown). Nevertheless, TE_p, A_p, and A_y remain the primary contributors to the enhanced warming in the Arctic 14-km model. This suggests that transient vertical motions continue to play a key role in driving the temperature and associated dynamical response differences between the two resolutions.

4. Summary and discussion

a. Summary

In this study, we conducted PAMIP-type Arctic sea ice loss experiments using two configurations of the global CAM6 atmospheric model: one at a horizontal resolution of 110 km and the other with regional refinement of 14 km over the Arctic. Previous studies have shown that simulated precipitation is highly sensitive to horizontal resolution via linkages to vertical motion (e.g., Herrington and Reed 2020). Here, we investigate how the atmospheric response to Arctic sea ice loss varies across horizontal resolutions and examine the underlying mechanisms. Our results are based on 100-member ensembles of preindustrial (1850–69) and future (2080–99) Arctic sea ice conditions for the Arctic 14-km model and 600-member ensembles for the global 110-km model. Our main findings can be summarized as follows.

1) The projected increase in Arctic precipitation during boreal winter is strongly influenced by sea ice loss, which enhances local moisture availability through increased upward latent heat fluxes as newly ice-free surfaces become exposed to the atmosphere.
2) The increase in Arctic precipitation in response to sea ice loss is more pronounced at higher horizontal resolution. This can be understood through changes in upward moisture fluxes. In both model resolutions, higher Arctic moisture availability leads to more frequent low-intensity precipitation events, increasing total precipitation. Additionally, the stronger upward motion in the high-resolution model compared to the low-resolution model results in more higher-intensity precipitation events and fewer lower-intensity precipitation events, further amplifying the total precipitation increase.
3) Beyond the mean precipitation response, sea ice loss also enhances daily precipitation variability in the Arctic. This increase is more than twice as large in the Arctic 14-km model compared to the global 110-km model and is closely linked to daily variability in vertical motion.

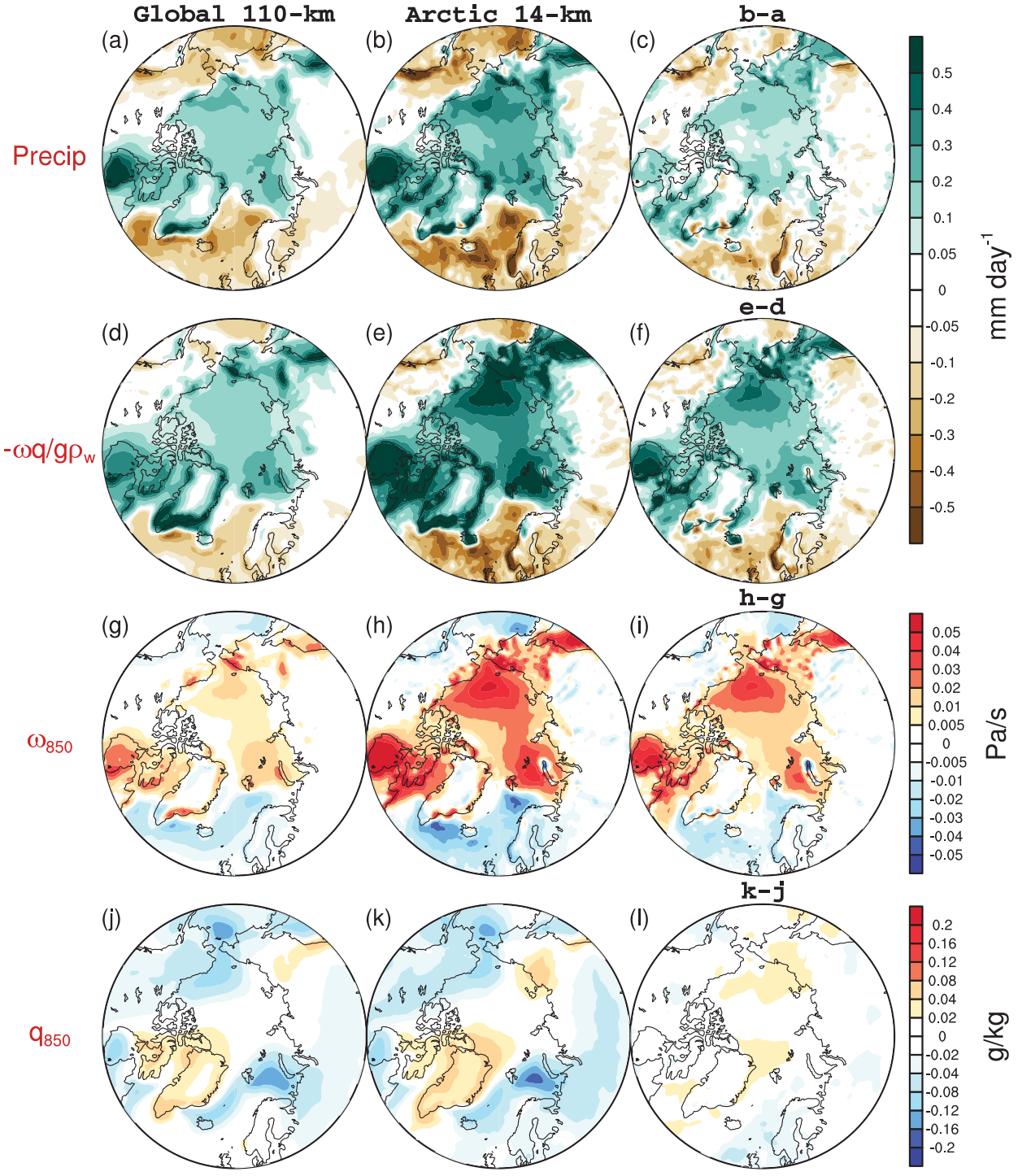

FIG. 8. Daily standard deviation response to Arctic sea ice loss in (left) global 110-km, (middle) Arctic 14-km, and (right) their difference for (first row) total precipitation, (second row) upward moisture flux at 850 hPa, (third row) vertical motion, and (fourth row) moisture.

4) The Arctic 14-km model exhibits greater polar cap warming throughout the troposphere (peaking near 800 hPa) compared to the global 110-km model, accompanied by a 50% stronger deceleration of the zonal-mean zonal winds around 60°–80°N. The enhanced response in the Arctic 14-km model compared to the global 110-km model is not attributable to noise, given the smaller ensemble size, as shown by a bootstrapping analysis based on resampling.

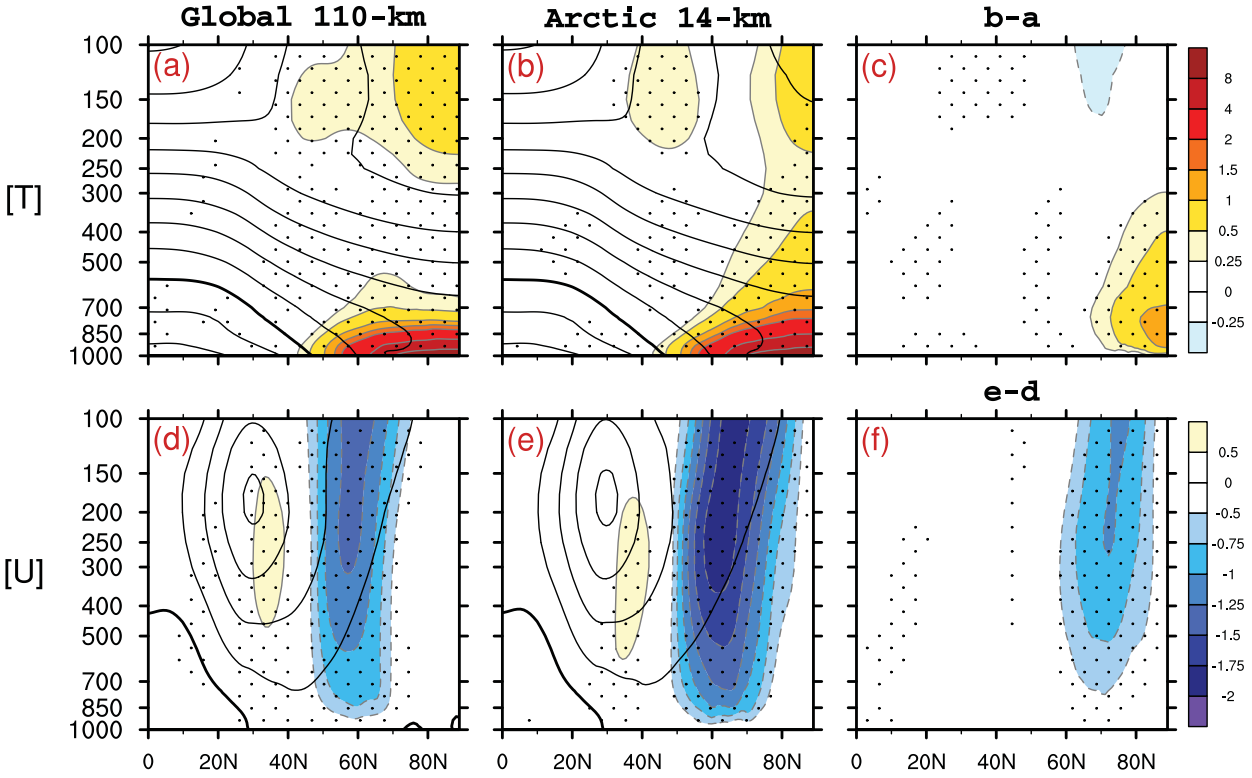

FIG. 9. Shading: responses of December–March (top) zonal-mean temperature (°C) and (bottom) zonal wind (m s^{-1}) to Arctic sea ice loss in (left) global 110-km, (middle) Arctic 14-km, and (right) their difference. Contours show the climatology with the interval of 10°C and 10 m s^{-1}. Stippling indicates regions where the ensemble-mean difference is statistically significant at the 95% confidence level based on the two-sided Student's *t* test.

The thermodynamic budget analysis suggests that the additional warming in the high-resolution model is linked to vertical heat transport, particularly by transient eddies.

Collectively, these results highlight the sensitivity of Arctic precipitation and atmospheric circulation responses to sea ice loss across different horizontal resolutions. They also suggest that vertical motion plays a crucial role in driving this sensitivity.

b. Discussion

The relative contributions of local evaporation and remote moisture transport to future Arctic precipitation changes remain an active area of research. Leister et al. (2025) examined late-twenty-first-century Arctic precipitation using both fully coupled and atmosphere-only CESM configurations and indicated that enhanced evaporation over newly ice-free ocean is the leading contributor to the wintertime precipitation increase, with remote SST forcing playing a secondary role. Although our experiments do not isolate individual processes such as the direct radiative effect of carbon dioxide (CO_2) or nonlinear interactions arising from the coinfluence of local evaporation and remote moisture transport, our results are consistent with the mechanism identified by Leister et al. (2025). These comparisons reinforce that sea ice loss is an important, but not exclusive, factor shaping future Arctic precipitation changes.

Our results also highlight key factors related to the sensitivity of simulated precipitation and atmospheric circulation to horizontal resolution. First, precipitation sensitivity varies by precipitation type, and changes in different types can offset one another when considering total precipitation. This is consistent with previous findings that higher resolution tends to increase large-scale stratiform precipitation and reduce deep convective precipitation (Terai et al. 2018; Herrington and Reed 2020). In our experiments, the total precipitation response to Arctic sea ice loss increases modestly (8.5%) from the 110- to 14-km grid, but the response in large-scale precipitation increases more substantially (25%). This illustrates how resolution affects the partitioning among precipitation types, even if the overall mean response changes only slightly.

Second, our scaling and physical decomposition analyses suggest that the precipitation response to Arctic sea ice loss is thermodynamically driven, mainly due to increased moisture availability leading to more frequent low-intensity precipitation events. In contrast, the influence of horizontal resolution on both precipitation climatology and its response to Arctic sea ice loss across resolutions is more closely linked to vertical motion. At higher resolution, stronger vertical motion leads to fewer low-intensity precipitation events and more frequent higher-intensity precipitation events, resulting in an overall increase in both precipitation climatology and response. The increase in daily precipitation variability is also found to be

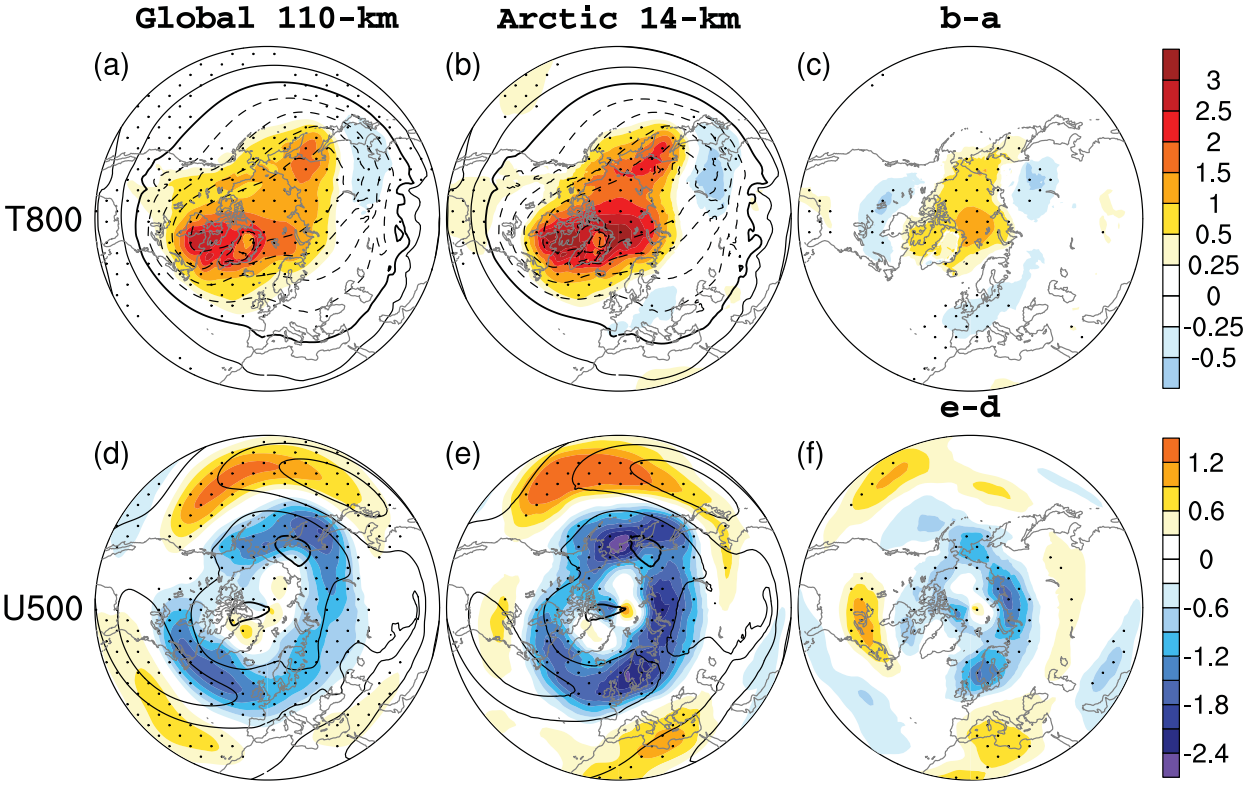

FIG. 10. As in Fig. 9, but for the responses in 800-hPa temperature (°C) and 500-hPa zonal wind (m s^{-1}) to Arctic sea ice loss in (left) global 110-km, (middle) Arctic 14-km, and (right) their difference. Contours show the climatology with the interval of 5°C and 10 m s^{-1}. Stippling indicates regions where the ensemble-mean difference is statistically significant at the 95% confidence level based on the two-sided Student's *t* test.

linked to increased vertical motion variability. Therefore, the resolution sensitivity of mean precipitation, precipitation variability, and their responses to sea ice loss are primarily dynamically driven.

It is also worth noting that the sensitivity to resolution manifests differently in daily precipitation variability and the mean precipitation response. The enhanced variability in the Arctic 14-km model closely corresponds to increased variability in vertical motion. By contrast, the amplified mean precipitation response cannot be attributed to changes in the mean vertical motion, which shows no systematic resolution dependence (not shown). Instead, as sea ice retreats and local moisture increases, the higher-resolution model permits a broader range of vertical velocities. This enables stronger upward moisture flux and more frequent high-intensity precipitation events, while the coarser model tends to produce more low-intensity events. This redistribution across precipitation intensity contributes to the enhanced mean response in the Arctic 14-km model.

Third, our results reveal an amplified response of polar tropospheric warming and associated zonal wind deceleration to Arctic sea ice loss at high resolution. However, most of this sensitivity is confined to high latitudes, with minimal extension south of ~30°N; further, the circulation response is distinct from the canonical NAO/NAM pattern. This latter point suggests that the eddy feedback mechanism proposed by Smith et al. (2022) does not account for the sensitivity observed here. Indeed, we find that the correlation between the eddy momentum flux convergence and the mean flow remains similar between global 110-km and Arctic 14-km resolutions (not shown). By comparison, Wills et al. (2024) found a stronger NAO response to Gulf Stream SST anomalies in a North Atlantic–refined 14-km model resulted from stronger heat fluxes by transient vertical motions, which we also found to be important for the response to Arctic sea ice loss. This suggests that higher resolution may be crucial for capturing the vertical fluxes important for large-scale atmospheric circulation responses to a wide range of surface anomalies.

Our primary goal is to assess the sensitivity of Arctic precipitation to horizontal resolution, but it is also instructive to compare our control simulations with reanalysis, despite the fact that the model is driven by preindustrial surface boundary forcing, which limits the fairness of the comparison. Figure S4 shows the PDF of daily mean precipitation in boreal winter (DJF) over the Arctic from ERA5 (Hersbach et al. 2020), the global 110-km model, and the Arctic 14-km model. ERA5, with a native resolution of ~31 km, assimilates observations but remains a model-based product, particularly in the data-sparse Arctic. We find that ERA5 exhibits stronger precipitation extremes than the global 110-km model, consistent with

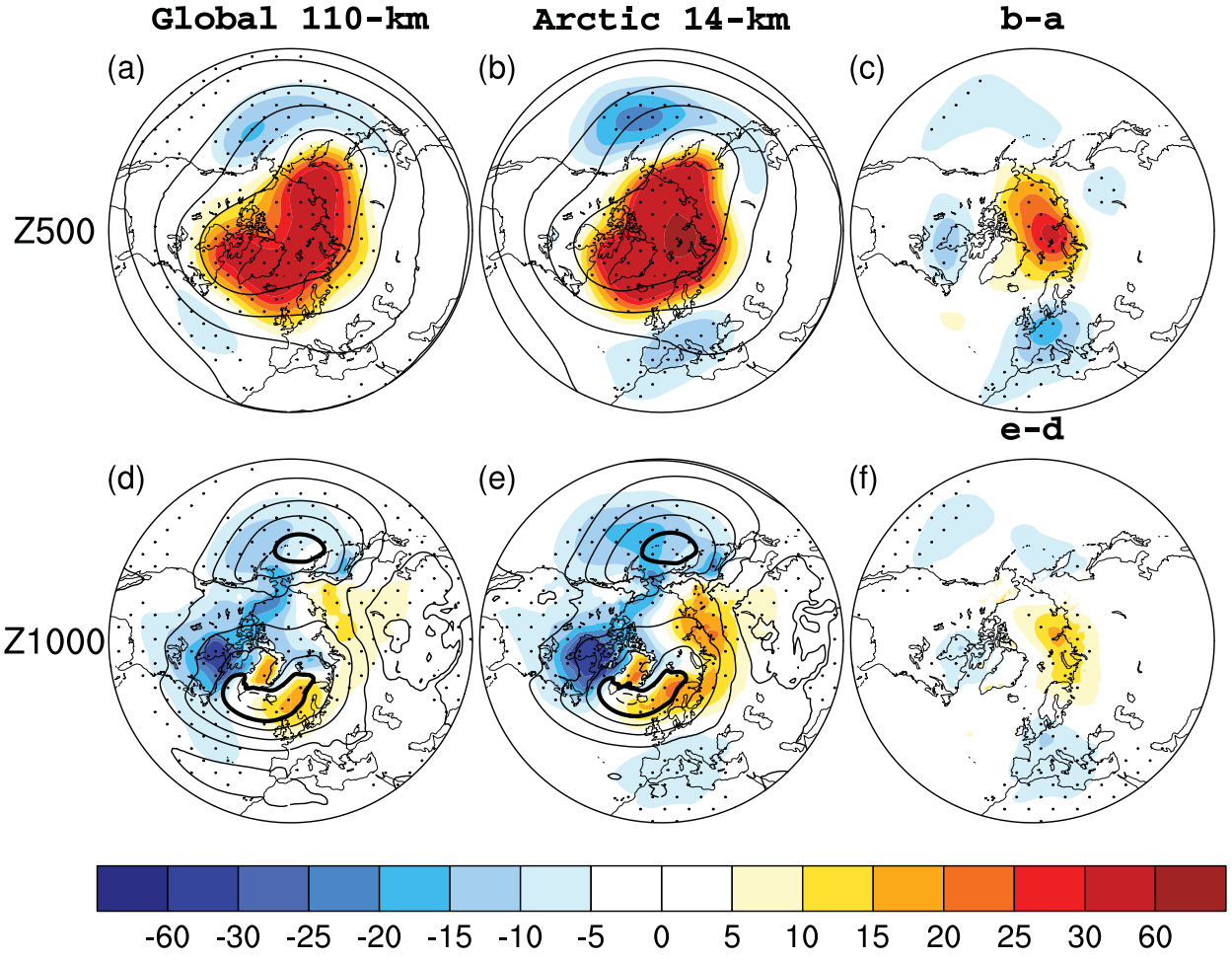

FIG. 11. As in Fig. 10, but for the geopotential height (gpm) response at 500 and 1000 hPa.

previous findings in Herrington et al. (2022), which showed that a regionally refined CESM configuration at ~28-km resolution better captured the intensity of high-latitude storms compared to a coarser 110-km model. Our Arctic 14-km model produces even stronger extremes than ERA5, which we interpret as a manifestation of its further resolution enhancement compared to ERA5 rather than overestimation. This comparison reinforces our conclusion that horizontal resolution plays a critical role in shaping both the distribution and the response of Arctic precipitation to sea ice loss.

Our results come with some limitations. First, our global 110-km sea ice experiments use the SE dynamical core, whereas CESM2-LE uses the finite volume (FV) dynamical core. Therefore, differences in response between the climate change scenario and the sea ice experiment (recall Fig. 2) could partly be due to the choice of dynamical cores, as shown in Jun et al. (2018). Second, the Arctic 14-km simulation exhibits a slightly weaker near-surface inversion compared to the global 110-km model, consistent with reduced static stability and a modestly higher planetary boundary layer height. Such thermodynamic differences could potentially enable a broader range of vertical velocity responses to sea ice loss, although the extent of this sensitivity remains uncertain and warrants dedicated investigation in future work.

Third, our experiments are conducted with an atmosphere-only model, which allows us to isolate the atmospheric response to prescribed Arctic sea ice loss but omits ocean feedbacks. Prior fully coupled studies highlight several large-scale oceanic adjustments outside the Arctic, including weakened Atlantic meridional overturning circulation (AMOC), large-scale SST warming, and an equatorward shift of the intertropical convergence zone (ITCZ), all of which are absent in our atmosphere-only setup (Deser et al. 2015). These SST and circulation changes can further warm the Arctic midtroposphere and enhance the Arctic precipitation response during winter (Deser et al. 2016; Blackport and Kushner 2018), although the magnitude of this effect remains uncertain because of potential artificial heating in the experimental protocol (England et al. 2022). Together, these omitted processes suggest that the sensitivity of the atmospheric response across horizontal resolutions may be even greater when ocean coupling is enabled. E3SM has the capability to run regionally refined Arctic configurations in fully coupled mode (Huo et al. 2025), making it well suited for exploring

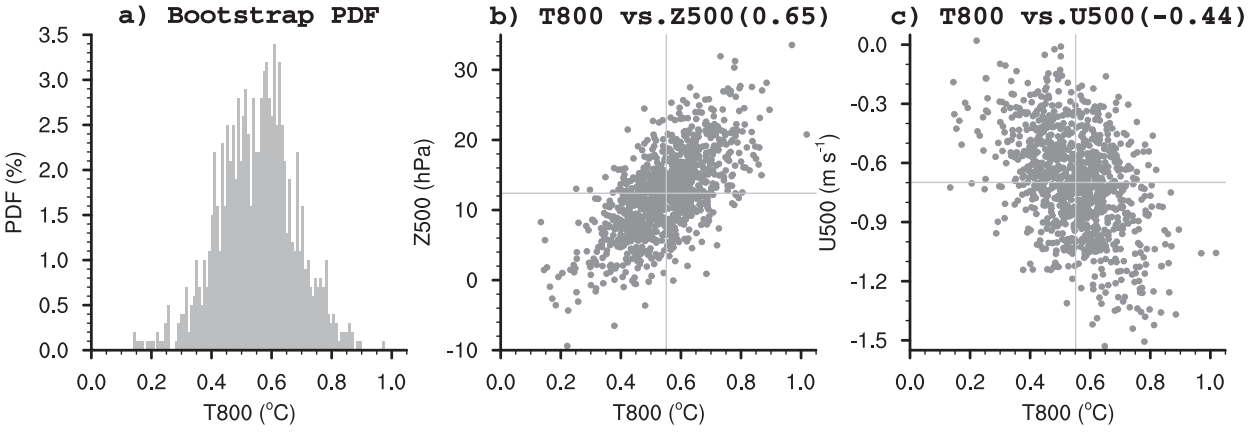

FIG. 12. (a) Histogram showing the bootstrapped distribution of the difference in polar-averaged (65°–90°N) temperature response at 800 hPa, based on random selection of 100 members from the global 110-km and Arctic 14-km simulations with replacement. (b) Scatterplot of the bootstrapped temperature response at 800 hPa vs the geopotential height response at 500 hPa, both averaged over the polar cap. (c) Scatterplot of the bootstrapped polar-averaged temperature response at 800 hPa vs the zonal wind response averaged over 65°–80°N at 500 hPa. Numbers in parentheses represent the correlation coefficients.

the sensitivity of Arctic precipitation to resolution and coupling complexity.

Despite this limitation, the utility of the atmosphere-only framework is supported by analysis of PAMIP simulations with CAM6 (Sun et al. 2022). These experiments show that Arctic precipitation increases are primarily driven by sea ice loss in regions with strong retreat, while global SST warming exerts a more uniform influence. The combined response closely matches the sum of the individual SST and sea ice effects, indicating a near-linear additivity. These results support the use of atmosphere-only models for isolating the influence of sea ice loss and quantifying its contribution to the broader climate response. In this novel context of the use of a regionally refined configuration to explore resolution impacts, setting up a tuned and balanced coupled version of this regionally refined grid would be a substantial task. While we recognize that work should continue to explore the impacts of coupling on these results, we consider the evidence presented in support of the use of atmosphere-only models to explore sea ice impacts to be sufficient motivation to consider this work as a reasonable step toward understanding resolution sensitivities.

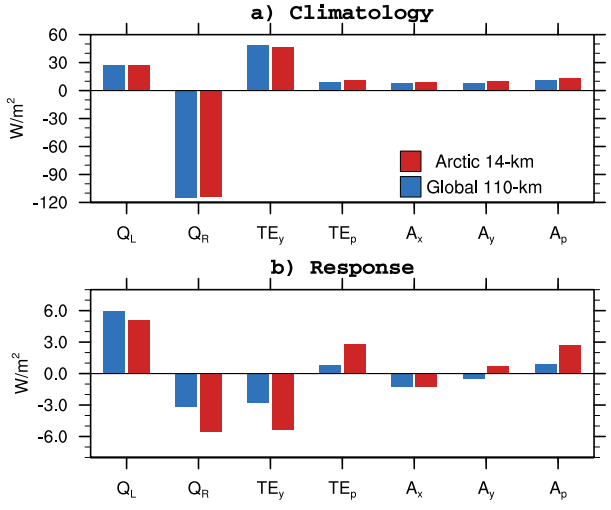

FIG. 13. Terms of the thermodynamic equation averaged over the Arctic midtroposphere (65°–90°N; 300–850 hPa). (a) Climatology in global 110-km and Arctic 14-km models. (b) Response to sea ice loss in global 110-km and Arctic 14-km models. See Eq. (6) for details of the individual terms.

Fourth, previous studies have shown that increasing both horizontal and vertical resolutions can improve the simulation of atmospheric processes (e.g., Skamarock et al. 2019; Streffing et al. 2021). We use the same 32 vertical levels in both configurations to isolate the impact of horizontal resolution without introducing changes in model physics or requiring retuning. Future versions of CESM, such as CESM3, with more boundary layer levels and higher free-tropospheric resolution, will allow further exploration of this issue. Last, our results are based on a single model, and some differences from Streffing et al. (2021) may reflect model dependence. Nonetheless, our study represents a step toward understanding resolution sensitivity and highlights its importance through physically plausible mechanisms. Conducting similar experiments with other climate models would be a valuable next step.

Acknowledgments. We acknowledge constructive discussions with Dr. Brian Medeiros (NSF-NCAR). C. D., A. R. H., and I. R. S. were supported by the NSF National Center for Atmospheric Research which is a major facility sponsored by the NSF under the Cooperative Agreement 1852977. High-performance computing support from Cheyenne was provided by NCAR's Computational and Information Systems Laboratory, sponsored by the NSF, through University Allocation UWAS0109 and NCAR allocation P04010022. L. S. was supported by NSF AGS-2300038. R. C. J. W. was supported by NSF AGS-2128409 and the Swiss National Science Foundation (Award PCEFP2 203376). M. G. was supported by NSF AGS-2236771. We thank

the three anonymous reviewers for their thoughtful and constructive comments, which helped to improve the manuscript.

Data availability statement. Postprocessed data for our PAMIP-type simulations in the Arctic 14-km and global 110-km models are available at https://doi.org/10.5281/zenodo.15367090.

REFERENCES

Anderson, B. T., N. Feldl, and B. R. Lintner, 2018: Emergent behavior of Arctic precipitation in response to enhanced Arctic warming. *J. Geophys. Res. Atmos.*, **123**, 2704–2717, https://doi.org/10.1002/2017JD026799.

Athanasiadis, P. J., and Coauthors, 2022: Mitigating climate biases in the midlatitude North Atlantic by increasing model resolution: SST gradients and their relation to blocking and the jet. *J. Climate*, **35**, 6985–7006, https://doi.org/10.1175/JCLI-D-21-0515.1.

Barnes, E. A., and J. A. Screen, 2015: The impact of Arctic warming on the midlatitude jet-stream: Can it? Has it? Will it? *Wiley Interdiscip. Rev.: Climate Change*, **6**, 277–286, https://doi.org/10.1002/wcc.337.

Bintanja, R., and F. M. Selten, 2014: Future increases in Arctic precipitation linked to local evaporation and sea-ice retreat. *Nature*, **509**, 479–482, https://doi.org/10.1038/nature13259.

——, K. van der Wiel, E. C. van der Linden, J. Reusen, L. Bogerd, F. Krikken, and F. M. Selten, 2020: Strong future increases in Arctic precipitation variability linked to poleward moisture transport. *Sci. Adv.*, **6**, eaax6869, https://doi.org/10.1126/sciadv.aax6869.

Black, R. X., B. A. McDaniel, and W. A. Robinson, 2006: Stratosphere–troposphere coupling during spring onset. *J. Climate*, **19**, 4891–4901, https://doi.org/10.1175/JCLI3907.1.

Blackport, R., and P. J. Kushner, 2018: The role of extratropical ocean warming in the coupled climate response to Arctic sea ice loss. *J. Climate*, **31**, 9193–9206, https://doi.org/10.1175/JCLI-D-18-0192.1.

——, and J. A. Screen, 2019: Influence of Arctic sea ice loss in autumn compared to that in winter on the atmospheric circulation. *Geophys. Res. Lett.*, **46**, 2213–2221, https://doi.org/10.1029/2018GL081469.

——, and ——, 2020: Weakened evidence for mid-latitude impacts of Arctic warming. *Nat. Climate Change*, **10**, 1065–1066, https://doi.org/10.1038/s41558-020-00954-y.

Bogenschutz, P. A., A. Gettelman, H. Morrison, V. E. Larson, C. Craig, and D. P. Schanen, 2013: Higher-order turbulence closure and its impact on climate simulations in the Community Atmosphere Model. *J. Climate*, **26**, 9655–9676, https://doi.org/10.1175/JCLI-D-13-00075.1.

Bonan, D. B., N. Feldl, M. D. Zelinka, and L. C. Hahn, 2023: Contributions to regional precipitation change and its polar-amplified pattern under warming. *Environ. Res. Climate*, **2**, 035010, https://doi.org/10.1088/2752-5295/ace27a.

Caldwell, P. M., and Coauthors, 2019: The DOE E3SM coupled model version 1: Description and results at high resolution. *J. Adv. Model. Earth Syst.*, **11**, 4095–4146, https://doi.org/10.1029/2019MS001870.

Chang, P., and Coauthors, 2020: An unprecedented set of high-resolution Earth system simulations for understanding multiscale interactions in climate variability and change. *J. Adv. Model. Earth Syst.*, **12**, e2020MS002298, https://doi.org/10.1029/2020MS002298.

Chen, X., and A. Dai, 2024: Quantifying contributions of external forcing and internal variability to Arctic warming during 1900–2021. *Earth's Future*, **12**, e2023EF003734, https://doi.org/10.1029/2023EF003734.

Cheng, K.-Y., and Coauthors, 2022: Impact of warmer sea surface temperature on the global pattern of intense convection: Insights from a global storm resolving model. *Geophys. Res. Lett.*, **49**, e2022GL099796, https://doi.org/10.1029/2022GL099796.

Cohen, J., and Coauthors, 2020: Divergent consensuses on Arctic amplification influence on midlatitude severe winter weather. *Nat. Climate Change*, **10**, 20–29, https://doi.org/10.1038/s41558-019-0662-y.

Craig, C., and Coauthors, 2021: CAM6.3 user's guide. NCAR Tech. Rep. NCAR/TN-571+EDD, 88 pp., https://doi.org/10.5065/Z953-ZC95.

Dai, A., and M. Song, 2020: Little influence of Arctic amplification on mid-latitude climate. *Nat. Climate Change*, **10**, 231–237, https://doi.org/10.1038/s41558-020-0694-3.

——, and M. T. Jenkins, 2023: Relationships among Arctic warming, sea-ice loss, stability, lapse rate feedback, and Arctic amplification. *Climate Dyn.*, **61**, 5217–5232, https://doi.org/10.1007/s00382-023-06848-x.

——, D. Luo, M. Song, and J. Liu, 2019: Arctic amplification is caused by sea-ice loss under increasing CO_2. *Nat. Commun.*, **10**, 121, https://doi.org/10.1038/s41467-018-07954-9.

Danabasoglu, G., and Coauthors, 2020: The Community Earth System Model version 2 (CESM2). *J. Adv. Model. Earth Syst.*, **12**, e2019MS001916, https://doi.org/10.1029/2019MS001916.

Deser, C., R. Tomas, M. Alexander, and D. Lawrence, 2010: The seasonal atmospheric response to projected Arctic sea ice loss in the late twenty-first century. *J. Climate*, **23**, 333–351, https://doi.org/10.1175/2009JCLI3053.1.

——, ——, and L. Sun, 2015: The role of ocean–atmosphere coupling in the zonal-mean atmospheric response to Arctic sea ice loss. *J. Climate*, **28**, 2168–2186, https://doi.org/10.1175/JCLI-D-14-00325.1.

——, L. Sun, R. A. Tomas, and J. Screen, 2016: Does ocean coupling matter for the northern extratropical response to projected Arctic sea ice loss? *Geophys. Res. Lett.*, **43**, 2149–2157, https://doi.org/10.1002/2016GL067792.

——, I. R. Simpson, K. A. McKinnon, and A. S. Phillips, 2017: The Northern Hemisphere extratropical atmospheric circulation response to ENSO: How well do we know it and how do we evaluate models accordingly? *J. Climate*, **30**, 5059–5082, https://doi.org/10.1175/JCLI-D-16-0844.1.

England, M. R., I. Eisenman, N. J. Lutsko, and T. J. W. Wagner, 2021: The recent emergence of Arctic Amplification. *Geophys. Res. Lett.*, **48**, e2021GL094086, https://doi.org/10.1029/2021GL094086.

——, ——, and T. J. W. Wagner, 2022: Spurious climate impacts in coupled sea ice loss simulations. *J. Climate*, **35**, 7401–7411, https://doi.org/10.1175/JCLI-D-21-0647.1.

ESMF Team, 2021: ESMF user guide. ESMF Tech. Rep., 78 pp.

Feldl, N., and T. M. Merlis, 2021: Polar amplification in idealized climates: The role of ice, moisture, and seasons. *Geophys. Res. Lett.*, **48**, e2021GL094130, https://doi.org/10.1029/2021GL094130.

——, S. Po-Chedley, H. K. A. Singh, S. Hay, and P. J. Kushner, 2020: Sea ice and atmospheric circulation shape the high-latitude lapse rate feedback. *npj Climate Atmos. Sci.*, **3**, 41, https://doi.org/10.1038/s41612-020-00146-7.

Fetterer, F., K. Knowles, W. N. Meier, M. Savoie, and A. K. Windnagel, 2017: Sea Ice Index. (G02135, version 3). National Snow and Ice Data Center, accessed 16 March 2025, https://doi.org/10.7265/N5K072F8.

Gettelman, A., and Coauthors, 2019: High climate sensitivity in the Community Earth System Model Version 2 (CESM2). *Geophys. Res. Lett.*, **46**, 8329–8337, https://doi.org/10.1029/2019GL083978.

Haarsma, R. J., and Coauthors, 2016: High Resolution Model Intercomparison Project (HighResMIP v1.0) for CMIP6. *Geosci. Model Dev.*, **9**, 4185–4208, https://doi.org/10.5194/gmd-9-4185-2016.

Hahn, L. C., K. C. Armour, M. D. Zelinka, C. M. Bitz, and A. Donohoe, 2021: Contributions to polar amplification in CMIP5 and CMIP6 models. *Front. Earth Sci.*, **9**, 710036, https://doi.org/10.3389/feart.2021.710036.

Harris, L., and Coauthors, 2020: GFDL SHiELD: A unified system for weather-to-seasonal prediction. *J. Adv. Model. Earth Syst.*, **12**, e2020MS002223, https://doi.org/10.1029/2020MS002223.

Hay, S., P. J. Kushner, R. Blackport, and K. E. McCusker, 2018: On the relative robustness of the climate response to high-latitude and low-latitude warming. *Geophys. Res. Lett.*, **45**, 6232–6241, https://doi.org/10.1029/2018GL077294.

——, and Coauthors, 2022: Separating the influences of low-latitude warming and sea ice loss on Northern Hemisphere climate change. *J. Climate*, **35**, 2327–2349, https://doi.org/10.1175/JCLI-D-21-0180.1.

Hersbach, H., and Coauthors, 2020: The ERA5 global reanalysis. *Quart. J. Roy. Meteor. Soc.*, **146**, 1999–2049, https://doi.org/10.1002/qj.3803.

Herrington, A. R., and K. A. Reed, 2017: An explanation for the sensitivity of the mean state of the Community Atmosphere Model to horizontal resolution on aquaplanets. *J. Climate*, **30**, 4781–4797, https://doi.org/10.1175/JCLI-D-16-0069.1.

——, and ——, 2018: An idealized test of the response of the Community Atmosphere Model to near-grid-scale forcing across hydrostatic resolutions. *J. Adv. Model. Earth Syst.*, **10**, 560–575, https://doi.org/10.1002/2017MS001078.

——, and ——, 2020: On resolution sensitivity in the Community Atmosphere Model. *Quart. J. Roy. Meteor. Soc.*, **146**, 3789–3807, https://doi.org/10.1002/qj.3873.

——, P. H. Lauritzen, M. Lofverstrom, W. H. Lipscomb, A. Gettelman, and M. A. Taylor, 2022: Impact of grids and dynamical cores in CESM2.2 on the surface mass balance of the Greenland Ice Sheet. *J. Adv. Model. Earth Syst.*, **14**, e2022MS003192, https://doi.org/10.1029/2022MS003192.

Hohenegger, C., and Coauthors, 2023: ICON-sapphire: Simulating the components of the Earth system and their interactions at kilometer and subkilometer scales. *Geosci. Model Dev.*, **16**, 779–811, https://doi.org/10.5194/gmd-16-779-2023.

Huang, X., A. Gettelman, W. C. Skamarock, P. H. Lauritzen, M. Curry, A. Herrington, J. T. Truesdale, and M. Duda, 2022: Advancing precipitation prediction using a new-generation storm-resolving model framework—SIMA-MPAS (V1.0): A case study over the western United States. *Geosci. Model Dev.*, **15**, 8135–8151, https://doi.org/10.5194/gmd-15-8135-2022.

Huo, Y., and Coauthors, 2025: E3SM-Arctic: Regionally refined coupled model for advanced understanding of Arctic systems interactions. *J. Adv. Model. Earth Syst.*, **17**, e2024MS004726, https://doi.org/10.1029/2024MS004726.

Hurrell, J. W., 1995: Decadal trends in the North Atlantic Oscillation: Regional temperatures and precipitation. *Science*, **269**, 676–679, https://doi.org/10.1126/science.269.5224.676.

Jeevanjee, N., and D. M. Romps, 2016: Effective buoyancy at the surface and aloft. *Quart. J. Roy. Meteor. Soc.*, **142**, 811–820, https://doi.org/10.1002/qj.2683.

Jenkins, M., and A. Dai, 2021: The impact of sea-ice loss on Arctic climate feedbacks and their role for Arctic amplification. *Geophys. Res. Lett.*, **48**, e2021GL094599, https://doi.org/10.1029/2021GL094599.

——, ——, and C. Deser, 2024: Arctic climate feedback response to local sea-ice concentration and remote sea surface temperature changes in PAMIP simulations. *Climate Dyn.*, **62**, 10 599–10 620, https://doi.org/10.1007/s00382-024-07465-y.

Jun, S.-Y., S.-J. Choi, and B.-M. Kim, 2018: Dynamical core in atmospheric model does matter in the simulation of Arctic climate. *Geophys. Res. Lett.*, **45**, 2805–2814, https://doi.org/10.1002/2018GL077478.

Kang, J. M., T. A. Shaw, and L. Sun, 2023: Arctic sea ice loss weakens Northern Hemisphere summertime storminess but not until the late 21st century. *Geophys. Res. Lett.*, **50**, e2022GL102301, https://doi.org/10.1029/2022GL102301.

Koenigk, T., M. Caian, G. Nikulin, and S. Schimanke, 2016: Regional Arctic sea ice variations as predictor for winter climate conditions. *Climate Dyn.*, **46**, 317–337, https://doi.org/10.1007/s00382-015-2586-1.

Labe, Z. M., 2020: The effects of Arctic sea-ice thickness loss and stratospheric variability on mid-latitude cold spells. Ph.D. dissertation, University of California, Irvine, 182 pp.

Larson, J. G., D. W. J. Thompson, and J. W. Hurrell, 2024: Signature of the western boundary currents in local climate variability. *Nature*, **634**, 862–867, https://doi.org/10.1038/s41586-024-08019-2.

Larson, V. E., J.-C. Golaz, and W. R. Cotton, 2002: Small-scale and mesoscale variability in cloudy boundary layers: Joint probability density functions. *J. Atmos. Sci.*, **59**, 3519–3539, https://doi.org/10.1175/1520-0469(2002)059%3C3519:SSAMVI%3E2.0.CO;2.

Lauritzen, P. H., and Coauthors, 2018: NCAR release of CAM-SE in CESM2.0: A reformulation of the spectral element dynamical core in dry-mass vertical coordinates with comprehensive treatment of condensates and energy. *J. Adv. Model. Earth Syst.*, **10**, 1537–1570, https://doi.org/10.1029/2017MS001257.

Leister, S. D., J. E. Kay, and C. Hannay, 2025: Local and remote moisture sources both increase late twenty-first century Arctic precipitation. *J. Climate*, **38**, 2963–2973, https://doi.org/10.1175/JCLI-D-24-0359.1.

Liang, Y.-C., and Coauthors, 2024: The weakening of the stratospheric polar vortex and the subsequent surface impacts as consequences to Arctic sea ice loss. *J. Climate*, **37**, 309–333, https://doi.org/10.1175/JCLI-D-23-0128.1.

——, O. Miyawaki, T. A. Shaw, I. Mitevski, L. M. Polvani, and Y.-T. Hwang, 2025: Linking radiative-advective equilibrium regime transition to Arctic amplification. *Geophys. Res. Lett.*, **52**, e2024GL113417, https://doi.org/10.1029/2024GL113417.

Lin, M., and Coauthors, 2024: The GFDL variable-resolution global chemistry-climate model for research at the nexus of US climate and air quality extremes. *J. Adv. Model. Earth Syst.*, **16**, e2023MS003984, https://doi.org/10.1029/2023MS003984.

Liu, W., P. A. Ullrich, J. Li, C. Zarzycki, P. M. Caldwell, L. R. Leung, and Y. Qian, 2023: The June 2012 North American derecho: A testbed for evaluating regional and global climate

modeling systems at cloud-resolving scales. *J. Adv. Model. Earth Syst.*, **15**, e2022MS003358, https://doi.org/10.1029/2022MS003358.

Lu, J., G. Chen, L. R. Leung, D. A. Burrows, Q. Yang, K. Sakaguchi, and S. Hagos, 2015: Toward the dynamical convergence on the jet stream in aquaplanet AGCMs. *J. Climate*, **28**, 6763–6782, https://doi.org/10.1175/JCLI-D-14-00761.1.

McCusker, K. E., P. J. Kushner, J. C. Fyfe, M. Sigmond, V. V. Kharin, and C. M. Bitz, 2017: Remarkable separability of circulation response to Arctic sea ice loss and greenhouse gas forcing. *Geophys. Res. Lett.*, **44**, 7955–7964, https://doi.org/10.1002/2017GL074327.

Meier, W. N., and J. Stroeve, 2022: An updated assessment of the changing Arctic sea ice cover. *Oceanography*, **35** (3–4), 10–19, https://doi.org/10.5670/oceanog.2022.114.

Moreno-Chamarro, E., and Coauthors, 2022: Impact of increased resolution on long-standing biases in HighResMIP-PRIMAVERA climate models. *Geosci. Model Dev.*, **15**, 269–289, https://doi.org/10.5194/gmd-15-269-2022.

Mori, M., M. Watanabe, H. Shiogama, J. Inoue, and M. Kimoto, 2014: Robust Arctic sea-ice influence on the frequent Eurasian cold winters in past decades. *Nat. Geosci.*, **7**, 869–873, https://doi.org/10.1038/ngeo2277.

Morris, M., P. J. Kushner, G. W. K. Moore, and O. Mercan, 2024: Resolution dependence of extreme wind speed projections in the Great Lakes region. *J. Climate*, **37**, 3153–3171, https://doi.org/10.1175/JCLI-D-23-0547.1.

Mudelsee, M., 2010: *Climate Time Series Analysis: Classical Statistical and Bootstrap Methods.* 1st ed. Springer, 474 pp.

Notz, D., and SIMIP Community, 2020: Arctic sea ice in CMIP6. *Geophys. Res. Lett.*, **47**, e2019GL086749, https://doi.org/10.1029/2019GL086749.

O'Brien, T. A., W. D. Collins, K. Kashinath, O. Rübel, S. Byna, J. Gu, H. Krishnan, and P. A. Ullrich, 2016: Resolution dependence of precipitation statistical fidelity in hindcast simulations. *J. Adv. Model. Earth Syst.*, **8**, 976–990, https://doi.org/10.1002/2016MS000671.

Osborne, J. M., J. A. Screen, and M. Collins, 2017: Ocean–atmosphere state dependence of the atmospheric response to Arctic sea ice loss. *J. Climate*, **30**, 1537–1552, https://doi.org/10.1175/jcli-d-16-0531.1.

Patrizio, C. R., P. J. Athanasiadis, C. Frankignoul, D. Iovino, S. Masina, L. Famooss Paolini, and S. Gualdi, 2023: Improved extratropical North Atlantic atmosphere–ocean variability with increasing ocean model resolution. *J. Climate*, **36**, 8403–8424, https://doi.org/10.1175/JCLI-D-23-0230.1.

Peings, Y., and G. Magnusdottir, 2014: Response of the wintertime Northern Hemisphere atmospheric circulation to current and projected Arctic sea ice decline: A numerical study with CAM5. *J. Climate*, **27**, 244–264, https://doi.org/10.1175/JCLI-D-13-00272.1.

——, Z. M. Labe, and G. Magnusdottir, 2021: Are 100 ensemble members enough to capture the remote atmospheric response to +2°C Arctic sea ice loss? *J. Climate*, **34**, 3751–3769, https://doi.org/10.1175/JCLI-D-20-0613.1.

Pendergrass, A. G., R. Knutti, F. Lehner, C. Deser, and B. M. Sanderson, 2017: Precipitation variability increases in a warmer climate. *Sci. Rep.*, **7**, 17966, https://doi.org/10.1038/s41598-017-17966-y.

Pithan, F., and T. Mauritsen, 2014: Arctic amplification dominated by temperature feedbacks in contemporary climate models. *Nat. Geosci.*, **7**, 181–184, https://doi.org/10.1038/ngeo2071.

——, and T. Jung, 2021: Arctic amplification of precipitation changes—The energy hypothesis. *Geophys. Res. Lett.*, **48**, e2021GL094977, https://doi.org/10.1029/2021GL094977.

Previdi, M., K. L. Smith, and L. M. Polvani, 2021: Arctic amplification of climate change: A review of underlying mechanisms. *Environ. Res. Lett.*, **16**, 093003, https://doi.org/10.1088/1748-9326/ac1c29.

Rackow, T., and Coauthors, 2025: Multi-year simulations at kilometre scale with the Integrated Forecasting System coupled to FESOM2.5/NEMOv3.4. *Geosci. Model Dev.*, **18**, 33–69, https://doi.org/10.5194/gmd-18-33-2025.

Randall, D. A., and K. Emanuel, 2024: The weather–climate schism. *Bull. Amer. Meteor. Soc.*, **105**, E300–E305, https://doi.org/10.1175/BAMS-D-23-0124.1.

Rantanen, M., A. Y. Karpechko, A. Lipponen, K. Nordling, O. Hyvärinen, K. Ruosteenoja, T. Vihma, and A. Laaksonen, 2022: The Arctic has warmed nearly four times faster than the globe since 1979. *Commun. Earth Environ.*, **3**, 168, https://doi.org/10.1038/s43247-022-00498-3.

Rasmussen, R. M., and Coauthors, 2023: CONUS404: The NCAR–USGS 4-km long-term regional hydroclimate reanalysis over the CONUS. *Bull. Amer. Meteor. Soc.*, **104**, E1382–E1408, https://doi.org/10.1175/BAMS-D-21-0326.1.

Rauscher, S. A., T. A. O'Brien, C. Piani, E. Coppola, F. Giorgi, W. D. Collins, and P. M. Lawston, 2016: A multimodel intercomparison of resolution effects on precipitation: Simulations and theory. *Climate Dyn.*, **47**, 2205–2218, https://doi.org/10.1007/s00382-015-2959-5.

Rhoades, A. M., X. Huang, P. A. Ullrich, and C. M. Zarzycki, 2016: Characterizing Sierra Nevada snowpack using variable-resolution CESM. *J. Appl. Meteor. Climatol.*, **55**, 173–196, https://doi.org/10.1175/JAMC-D-15-0156.1.

Roberts, M. J., and Coauthors, 2025: High-Resolution Model Intercomparison Project phase 2 (HighResMIP2) towards CMIP7. *Geosci. Model Dev.*, **18**, 1307–1332, https://doi.org/10.5194/gmd-18-1307-2025.

Rodgers, K. B., and Coauthors, 2021: Ubiquity of human-induced changes in climate variability. *Earth Syst. Dyn.*, **12**, 1393–1411, https://doi.org/10.5194/esd-12-1393-2021.

Ronalds, B., E. A. Barnes, R. Eade, Y. Peings, and M. Sigmond, 2020: North Pacific zonal wind response to sea ice loss in the Polar Amplification Model Intercomparison Project and its downstream implications. *Climate Dyn.*, **55**, 1779–1792, https://doi.org/10.1007/s00382-020-05352-w.

Royer, J. F., S. Planton, and M. Déqué, 1990: A sensitivity experiment for the removal of Arctic sea ice with the French spectral general circulation model. *Climate Dyn.*, **5**, 1–17, https://doi.org/10.1007/BF00195850.

Satoh, M., T. Matsuno, H. Tomita, H. Miura, T. Nasuno, and S.-I. Iga, 2008: Nonhydrostatic icosahedral atmospheric model (NICAM) for global cloud resolving simulations. *J. Comput. Phys.*, **227**, 3486–3514, https://doi.org/10.1016/j.jcp.2007.02.006.

Screen, J. A., and I. Simmonds, 2010: The central role of diminishing sea ice in recent Arctic temperature amplification. *Nature*, **464**, 1334–1337, https://doi.org/10.1038/nature09051.

——, ——, C. Deser, and R. Tomas, 2013: The atmospheric response to three decades of observed Arctic sea ice loss. *J. Climate*, **26**, 1230–1248, https://doi.org/10.1175/JCLI-D-12-00063.1.

——, C. Deser, I. Simmonds, and R. Tomas, 2014: Atmospheric impacts of Arctic sea-ice loss, 1979–2009: Separating forced change from atmospheric internal variability. *Climate Dyn.*, **43**, 333–344, https://doi.org/10.1007/s00382-013-1830-9.

——, and Coauthors, 2018: Consistency and discrepancy in the atmospheric response to Arctic sea-ice loss across climate models. *Nat. Geosci.*, **11**, 155–163, https://doi.org/10.1038/s41561-018-0059-y.

——, R. Eade, D. M. Smith, S. Thomson, and H. Yu, 2022: Net equatorward shift of the jet streams when the contribution from sea-ice loss is constrained by observed eddy feedback. *Geophys. Res. Lett.*, **49**, e2022GL100523, https://doi.org/10.1029/2022GL100523.

Segura, H., and Coauthors, 2025: nextGEMS: Entering the era of kilometer-scale Earth system modeling. *Geosci. Model Dev.*, **18**, 7735–7761, https://doi.org/10.5194/gmd-18-7735-2025.

Serreze, M. C., A. P. Barrett, J. C. Stroeve, D. N. Kindig, and M. M. Holland, 2009: The emergence of surface-based Arctic amplification. *Cryosphere*, **3**, 11–19, https://doi.org/10.5194/tc-3-11-2009.

——, S. Bigalke, R. Lader, A. Crawford, and T. J. Ballinger, 2024: Precipitation: Arctic Report Card: Update for 2024. NOAA Tech. Rep. OAR ARC 24-03, 8 pp.

Sigmond, M., and L. Sun, 2024: The role of the basic state in the climate response to future Arctic sea ice loss. *Environ. Res. Climate*, **3**, 031002, https://doi.org/10.1088/2752-5295/ad44ca.

Simon, A., G. Gastineau, C. Frankignoul, V. Lapin, and P. Ortega, 2022: Pacific Decadal Oscillation modulates the Arctic sea-ice loss influence on the midlatitude atmospheric circulation in winter. *Wea. Climate Dyn.*, **3**, 845–861, https://doi.org/10.5194/wcd-3-845-2022.

Simpson, I. R., and Coauthors, 2020: An evaluation of the large-scale atmospheric circulation and its variability in CESM2 and other CMIP models. *J. Geophys. Res. Atmos.*, **125**, e2020JD032835, https://doi.org/10.1029/2020JD032835.

Skamarock, W. C., C. Snyder, J. B. Klemp, and S. Park, 2019: Vertical resolution requirements in atmospheric simulation. *Mon. Wea. Rev.*, **147**, 2641–2656, https://doi.org/10.1175/MWR-D-19-0043.1.

Smirnov, D., M. Newman, M. A. Alexander, Y. Kwon, and C. Frankignoul, 2015: Investigating the local atmospheric response to a realistic shift in the Oyashio sea surface temperature front. *J. Climate*, **28**, 1126–1147, https://doi.org/10.1175/JCLI-D-14-00285.1.

Smith, D. M., N. J. Dunstone, A. A. Scaife, E. K. Fiedler, D. Copsey, and S. C. Hardiman, 2017: Atmospheric response to Arctic and Antarctic sea ice: The importance of ocean–atmosphere coupling and the background state. *J. Climate*, **30**, 4547–4565, https://doi.org/10.1175/JCLI-D-16-0564.1.

——, and Coauthors, 2019: The Polar Amplification Model Intercomparison Project (PAMIP) contribution to CMIP6: Investigating the causes and consequences of polar amplification. *Geosci. Model Dev.*, **12**, 1139–1164, https://doi.org/10.5194/gmd-12-1139-2019.

——, and Coauthors, 2022: Robust but weak winter atmospheric circulation response to future Arctic sea ice loss. *Nat. Commun.*, **13**, 727, https://doi.org/10.1038/s41467-022-28283-y.

Streffing, J., T. Semmler, L. Zampieri, and T. Jung, 2021: Response of Northern Hemisphere weather and climate to Arctic sea ice decline: Resolution independence in Polar Amplification Model Intercomparison Project (PAMIP) simulations. *J. Climate*, **34**, 8445–8457, https://doi.org/10.1175/JCLI-D-19-1005.1.

Stuecker, M. F., and Coauthors, 2018: Polar amplification dominated by local forcing and feedbacks. *Nat. Climate Change*, **8**, 1076–1081, https://doi.org/10.1038/s41558-018-0339-y.

Sun, L., C. Deser, and R. A. Tomas, 2015: Mechanisms of stratospheric and tropospheric circulation response to projected Arctic sea ice loss. *J. Climate*, **28**, 7824–7845, https://doi.org/10.1175/JCLI-D-15-0169.1.

——, J. Perlwitz, and M. Hoerling, 2016: What caused the recent "Warm Arctic, Cold Continents" trend pattern in winter temperatures? *Geophys. Res. Lett.*, **43**, 5345–5352, https://doi.org/10.1002/2016GL069024.

——, C. Deser, I. Simpson, and M. Sigmond, 2022: Uncertainty in the winter tropospheric response to Arctic sea ice loss: The role of stratospheric polar vortex internal variability. *J. Climate*, **35**, 3109–3130, https://doi.org/10.1175/JCLI-D-21-0543.1.

——, C. Patrizio, D. W. J. Thompson, and J. W. Hurrell, 2025: Influence of anomalous ocean heat transport on the extratropical atmospheric circulation in a high-resolution slab-ocean coupled model. *Geophys. Res. Lett.*, **52**, e2024GL111770, https://doi.org/10.1029/2024GL111770.

Sweeney, A. J., Q. Fu, S. Po-Chedley, H. Wang, and M. Wang, 2023: Internal variability increased Arctic Amplification during 1980–2022. *Geophys. Res. Lett.*, **50**, e2023GL106060, https://doi.org/10.1029/2023GL106060.

——, ——, ——, ——, and ——, 2024: Unique temperature trend pattern associated with internally driven Global Cooling and Arctic Warming during 1980–2022. *Geophys. Res. Lett.*, **51**, e2024GL108798, https://doi.org/10.1029/2024GL108798.

Tang, Q., and Coauthors, 2023: The fully coupled regionally refined model of E3SM version 2: Overview of the atmosphere, land, and river results. *Geosci. Model Dev.*, **16**, 3953–3995, https://doi.org/10.5194/gmd-16-3953-2023.

Taylor, P. C., and Coauthors, 2022: Process drivers, inter-model spread, and the path forward: A review of amplified Arctic warming. *Front. Earth Sci.*, **9**, 758361, https://doi.org/10.3389/feart.2021.758361.

Terai, C. R., P. M. Caldwell, S. A. Klein, Q. Tang, and M. L. Branstetter, 2018: The atmospheric hydrologic cycle in the ACME v0.3 model. *Climate Dyn.*, **50**, 3251–3279, https://doi.org/10.1007/s00382-017-3803-x.

Thompson, D. W. J., and J. M. Wallace, 2000: Annular modes in the extratropical circulation. Part I: Month-to-month variability. *J. Climate*, **13**, 1000–1016, https://doi.org/10.1175/1520-0442(2000)013<1000:amitec>2.0.co;2.

Wijngaard, R. R., W. J. van de Berg, C. T. van Dalum, A. R. Herrington, and X. J. Levine, 2025: Arctic temperature and precipitation extremes in present-day and future storyline-based variable resolution Community Earth System Model simulations. *Wea. Climate Dyn.*, **6**, 1241–1266, https://doi.org/10.5194/wcd-6-1241-2025.

Williams, N. C., A. A. Scaife, and J. A. Screen, 2024: Effect of increased ocean resolution on model errors in El Niño–Southern Oscillation and its teleconnections. *Quart. J. Roy. Meteor. Soc.*, **150**, 1489–1500, https://doi.org/10.1002/qj.4655.

Wills, R. C. J., A. R. Herrington, I. R. Simpson, and D. S. Battisti, 2024: Resolving weather fronts increases the large-scale circulation response to Gulf Stream SST anomalies in variable-resolution CESM2 simulations. *J. Adv. Model. Earth Syst.*, **16**, e2023MS004123, https://doi.org/10.1029/2023MS004123.

Xu, G., and Coauthors, 2024: High-resolution modelling identifies the Bering Strait's role in amplified Arctic warming. *Nat. Climate Change*, **14**, 615–622, https://doi.org/10.1038/s41558-024-02008-z.

Ye, K., T. Woollings, and S. N. Sparrow, 2024: Dynamic and thermodynamic control of the response of winter climate and extreme weather to projected Arctic sea-ice loss. *Geophys. Res. Lett.*, **51**, e2024GL109271, https://doi.org/10.1029/2024GL109271.

Yeager, S. G., and Coauthors, 2023: Reduced Southern Ocean warming enhances global skill and signal-to-noise in an eddy-resolving decadal prediction system. *npj Climate Atmos. Sci.*, **6**, 107, https://doi.org/10.1038/s41612-023-00434-y.

Yu, H., J. A. Screen, M. Xu, S. Hay, and J. L. Catto, 2024: Comparing the atmospheric responses to reduced Arctic sea ice, a warmer ocean, and increased CO_2 and their contributions to projected change at 2°C global warming. *J. Climate*, **37**, 6367–6380, https://doi.org/10.1175/JCLI-D-24-0104.1.

Yukimoto, S., N. Oshima, H. Kawai, M. Deushi, and T. Aizawa, 2024: Factors contributing to historical and future trends in Arctic precipitation. *Geophys. Res. Lett.*, **51**, e2023GL107467, https://doi.org/10.1029/2023GL107467.

Zarzycki, C. M., M. N. Levy, C. Jablonowski, J. R. Overfelt, M. A. Taylor, and P. A. Ullrich, 2014: Aquaplanet experiments using CAM's variable-resolution dynamical core. *J. Climate*, **27**, 5481–5503, https://doi.org/10.1175/JCLI-D-14-00004.1.

Zhang, P., Y. Wu, I. R. Simpson, K. L. Smith, X. Zhang, B. De, and P. Callaghan, 2018: A stratospheric pathway linking a colder Siberia to Barents-Kara Sea sea ice loss. *Sci. Adv.*, **4**, eaat6025, https://doi.org/10.1126/sciadv.aat6025.

Zheng, C., Y. Wu, M. Ting, J. A. Screen, and P. Zhang, 2023: Diverse Eurasian temperature responses to Arctic sea ice loss in models due to varying balance between dynamic cooling and thermodynamic warming. *J. Climate*, **36**, 8347–8364, https://doi.org/10.1175/JCLI-D-22-0937.1.

Zhou, W., L. Leung, S. Xie, and J. Lu, 2024: An analytic theory for the degree of Arctic Amplification. *Nat. Commun.*, **15**, 5060, https://doi.org/10.1038/s41467-024-48469-w.